Slowdown of Antarctic Bottom Water export driven by climatic wind and sea-ice changes

Shenjie Zhou, Andrew J. S. Meijers, Michael P. Meredith, E. Povl Abrahamsen, Paul R. Holland, Alessandro Silvano, Jean-Baptiste Sallée, Svein Østerhus

nature climate change

Article

https://doi.org/10.1038/s41558-023-01695-4

Slowdown of Antarctic Bottom Water export driven by climatic wind and sea-ice changes

Received: 16 June 2022

Accepted: 10 May 2023

Published online: 12 June 2023

Check for updates

Shenjie Zhou [1] ✉, Andrew J. S. Meijers [1], Michael P. Meredith [1], E. Povl Abrahamsen [1], Paul R. Holland [1], Alessandro Silvano [2], Jean-Baptiste Sallée [3] & Svein Østerhus [4]

Antarctic Bottom Water (AABW) is pivotal for oceanic heat and carbon sequestrations on multidecadal to millennial timescales. The Weddell Sea contributes nearly a half of global AABW through Weddell Sea Deep Water and denser underlying Weddell Sea Bottom Water that form on the continental shelves via sea-ice production. Here we report an observed 30% reduction of Weddell Sea Bottom Water volume since 1992, with the largest decrease in the densest classes. This is probably driven by a multidecadal reduction in dense-water production over southern continental shelf associated with a >40% decline in the sea-ice formation rate. The ice production decrease is driven by northerly wind trend, related to a phase transition of the Interdecadal Pacific Oscillation since the early 1990s, superposed by Amundsen Sea Low intrinsic variability. These results reveal key influences on exported AABW to the Atlantic abyss and their sensitivity to large-scale, multidecadal climate variability.

Antarctic Bottom Water (AABW) is the world's most voluminous water mass, comprising 30-40% of the volume of the global ocean[1]. AABW circulates from its formation sites around Antarctica throughout the global ocean as a part of the lower limb of the global overturning circulation[2] and plays a critical role in regulating Earth's climate by storing and transporting heat and carbon in the abyssal ocean[3,4]. The Weddell Sea is a key region for AABW production, being responsible for up to 50% of total AABW production[5]. The AABW that originates here renews the bottom layer of the Atlantic meridional overturning circulation and derives from dense waters formed in relatively small regions of the southwestern Weddell Sea continental shelf. In particular, the coastal polynyas in front of Ronne Ice Shelf and Berkner Bank[6,7] (Fig. 1) are important, where offshore sea-ice motion is consistently forced by cold and strong katabatic southerly winds off the ice shelf, maintaining open water and sustaining sea-ice production. In these regions, local wind, sea ice and coastal/seabed/ice-shelf geometry allow the continuous production and accumulation of High-Salinity Shelf Water (HSSW), formed from winter cooling and salinification by sea-ice formation.

A part of the HSSW formed near the Ronne Ice Shelf and Berkner Bank is directly exported northward and cascades down the continental slope over the western side of the southern Weddell continental shelf[8,9], mixing with mid-layer modified Warm Deep Water (WDW) on the slope before descending into the abyss of Weddell Sea. The other part of HSSW flows southwards underneath the Ronne Ice Shelf and is cooled and freshened through interaction with the Filchner–Ronne Ice Shelf (FRIS), leading to the formation of Ice Shelf Water with potential temperatures as low as −2.3 °C (refs. 8,10). The Ice Shelf Water contributes half of the total export of Dense Shelf Water (DSW)[9] from FRIS via the Filchner Depression to the abyssal Weddell Sea (Fig. 1). The DSW flows down the continental slope, entraining mid-layer modified WDW, forming the precursor water mass of Weddell Sea-origin AABW, named Weddell Sea Deep Water (WSDW), which is the densest water mass that can be directly exported from the Weddell Sea. It also produces the denser underlying Weddell Sea Bottom Water (WSBW)[4,11–14], which is largely retained within the Weddell basin but can modulate the properties of the exported AABW[14].

Over the past five decades, AABW around Antarctica has undergone a freshening and warming and a consequent volume reduction[14–18].

[1]British Antarctic Survey, Cambridge, UK. [2]Department of Ocean and Earth Science, National Oceanography Centre, University of Southampton, Southampton, UK. [3]Sorbonne Université, CNRS/IRD/MNHN, LOCEAN, IPSL, Paris, France. [4]NORCE Norwegian Research Centre and Bjerknes Centre for Climate Research, Bergen, Norway. ✉e-mail: shezhou@bas.ac.uk

https://doi.org/10.1038/s41558-023-01695-4

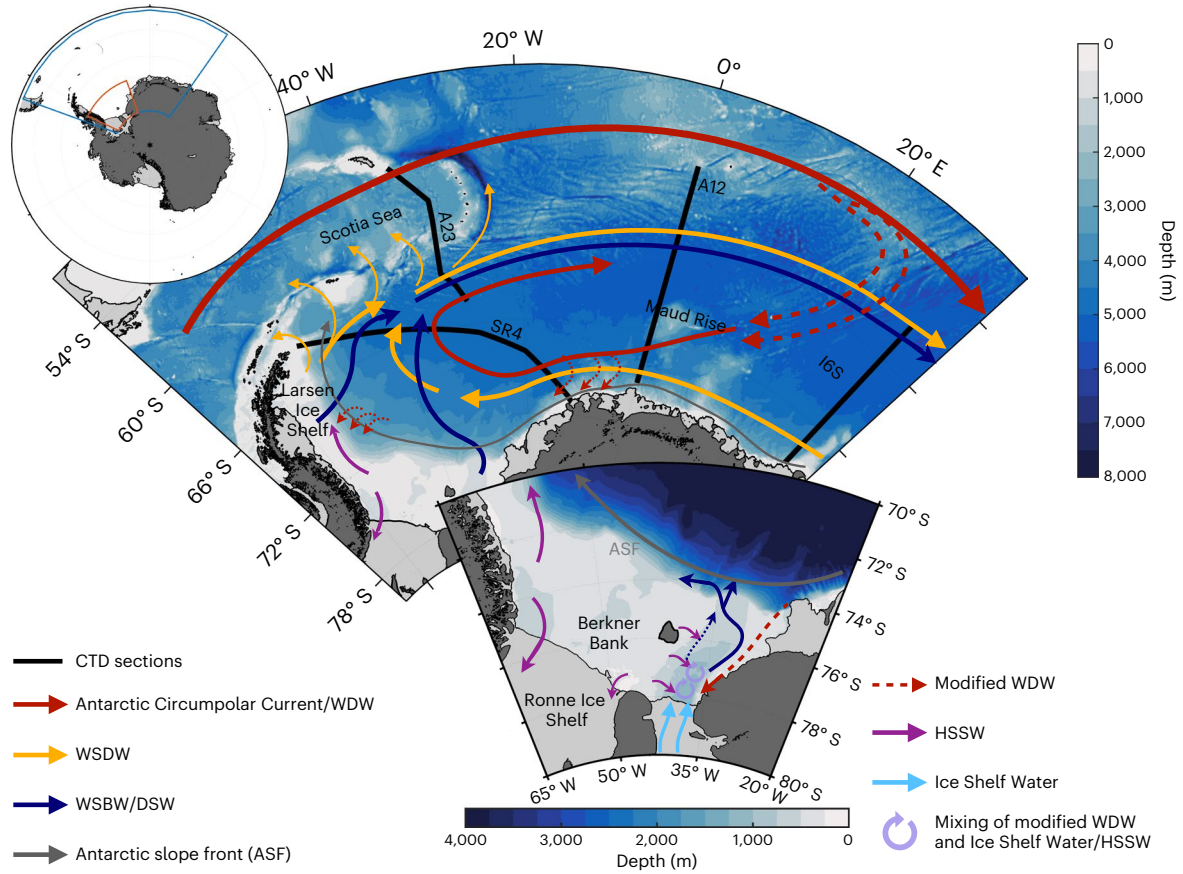

Fig. 1 | Pathways of water-mass circulation within the Weddell Sea and formation of WSBW on the shelf. The water masses within the Weddell Sea circulate around the cyclonic Weddell Gyre. WDW (red arrows) originating from the Antarctic Circumpolar Current enters the gyre from the northeast and flows towards the ice shelf. WSDW (yellow arrows) in the Weddell Sea is renewed from the input from the Indo-Pacific sector and is locally produced by the mixture of DSW and WDW. WSBW (dark blue arrows) in the Weddell Sea is sourced primarily from the southwestern continental shelf, where the HSSW (purple arrows) formed via sea-ice freezing is exported offshore from the western side of the Ronne Ice Shelf as well as spreading down to the FRIS, leading to Ice Shelf Water (light blue arrows) formation. DSW containing HSSW, Ice Shelf Water and a small portion of modified WDW descends into the Weddell basin while mixing with WDW to form WSBW. Three hydrographic transects—A12, SR4 and A23—are displayed in black lines, sitting on the Prime Meridian, across the gyre centre and over the northern boundary of the gyre, respectively. I6S transect sits further east at 30° E, marking the eastern boundary of Weddell Gyre. Temperature and salinity measurements collected by conductivity, temperature and depth (CTD) profilers are used to compute water mass area (Methods) shown in this study. The geographic locations of the Weddell Sea and southern Weddell continental shelf are marked in the inset circumpolar map with blue and red boxes, respectively.

The contraction of AABW is hypothesized to be the result of weakened AABW production, and hence a slowing in the lower limb of the meridional overturning circulation, hindering heat and carbon sequestration[17]. However, attribution of drivers for this change have been challenged by the sparsity of data from its formation sites and therefore is limited to conjecture. In the Indo-Pacific sector, this signal is tentatively attributed to the accelerating melting of the ice shelves in West Antarctica[15,19,20] and consequent freshening of HSSW source waters, while in the Atlantic sector, decadal AABW freshening observed near Drake Passage has been cautiously associated with the disintegration of the Larsen Ice Shelves[21]. The observed warming of Atlantic-sector AABW has likewise been linked to a possible reduced northward export of cold WSDW[22], and a multidecadal reduction in export of the coldest, densest classes of WSDW to the Scotia Sea has been recently observed and linked to a diminution of the underlying WSBW[14]. This volume reduction drives a deepening of the coldest variant of WSDW so that less of this water crosses the deep sills of the South Scotia Ridge separating the Weddell Sea and the Scotia Sea and Atlantic basin[14].

Both observations[23] and models[24,25] have emphasized the potential change in ocean–ice interaction at the FRIS under future climates, with the hypothesized presence of a tipping point under which WDW intrusion could trigger rapid ice-shelf melting[26]. However, FRIS has thus far been well protected by the presence of cold DSW, and there has been no evidence of increased basal melt forced by WDW intrusions[27,28], suggesting that the observed multidecadal reduction of WSBW is not related to increased freshwater release from the ice shelves but that other processes must be involved.

In this Article, we show a persistent, widespread WSBW volume decline and present evidence that this is driven by long-term sea-ice formation changes on the southern continental shelf of the Weddell Sea. Here the coastal polynya region has undergone a notable decrease in sea-ice divergence, driven by near-surface wind changes. In response, the formation of HSSW has been reduced, diminishing the supply of DSW to the WSBW. The trend in the surface winds that drives the sea-ice changes is partially associated with changes in modes of atmospheric variability, including links to the tropical Pacific Ocean. This suggests that a substantial fraction of the observed Weddell Sea wind trend is related to the Interdecadal Pacific Oscillation (IPO)[29]. The IPO has exhibited a transition from the positive phase to the negative phase since the early 1990s and is a signature of natural internal climate variability emanating from the tropical Pacific Ocean[30–32]. This suggests that a substantial fraction of observed changes in WSDW volume and export may be attributed to natural interdecadal variability of regional winds.

https://doi.org/10.1038/s41558-023-01695-4

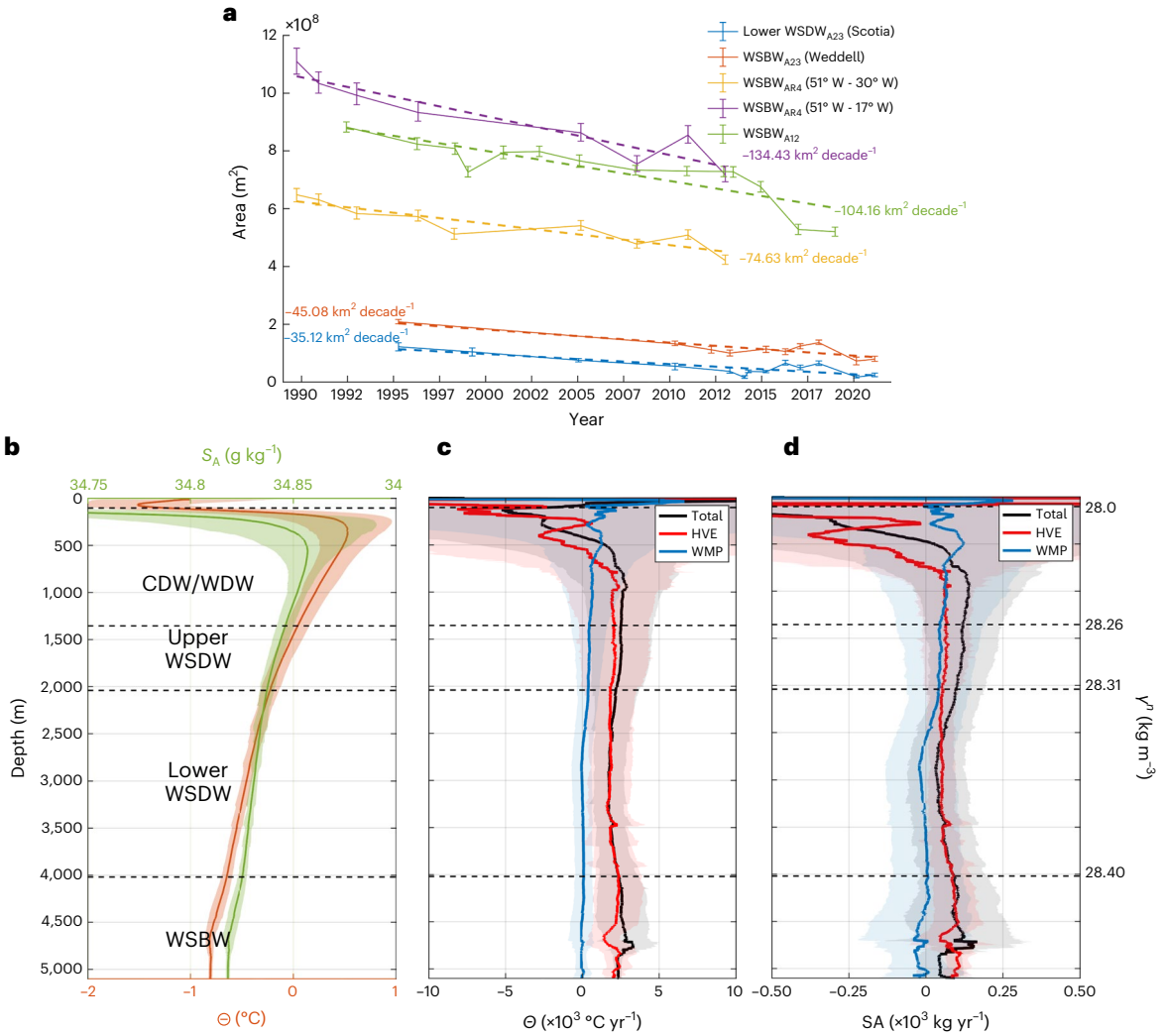

Fig. 2 | Basin-wide WSBW shrinkage and widespread deep Weddell Sea warming. a, The water-mass area along three hydrographic transects. The magnitude of linear trends estimated for each time series is shown in text with corresponding colour. WSBW areas computed along A12, SR4 and SR4 west (between 51° W and 30° W) and the Weddell Sea segment of A23 are illustrated, along with the WSDW area along the Scotia Sea part of A23. All the time series have statistically significant decreasing trends, with a notable connection between WSBW and Lower WSDW along A23. Error ranges are displayed and centred around the water-mass area as measured. The upper and lower bounds of error range account for combining the errors on neutral density field sourced from the instrumental uncertainties of both temperature (±0.001 °C) and salinity (±0.002) sensors. The lower bounds are the water-mass area when temperature measurements apply a 0.001 °C warming and salinity measurements apply a 0.002 freshening. The upper bounds are the water-mass area when temperature measurements apply a 0.001 °C cooling and salinity measurements apply a 0.002 salinification (Methods). **b**, The vertical temperature and salinity structure of the Weddell Sea averaged over A12, SR4 and the Weddell part of A23. Warm and saline Circumpolar Deep Water (CDW)/WDW overlies WSDW and WSBW with temperature and salinity decreasing with depth. Transparent shades denote ±1 standard deviation of temperature and salinity. **c**,**d**, The vertical structure of conservative temperature (**c**) and absolute salinity (**d**) trends averaged over all three transects. Total trends (black) are decomposed (Methods) into isopycnal heaving (HVE, red) and along-isopycnal water-mass property changes (WMP, blue). Shaded areas in **c** and **d** denote the 95% confidence level. Θ, conservative temperature; S_A, absolute salinity; γ^n, neutral density.

The long-term loss in WSBW volume

Temperature and salinity measurements collected from three repeat hydrographic transects—A12, SR4 and A23 (Fig. 1)—are used to quantify the area of WSBW water masses occupying each transect in different years, as an indicator of WSBW prevalence at the time of occupation. Transect A12 is located on the Prime Meridian and spans 69° S to 55° S across the western flank of Maud Rise. Transect SR4 crosses the Weddell Sea from Cape Norvegia on the coast of Queen Maud Land to Joinville Island at the tip of the Antarctic Peninsula. Transect A23 extends from the northern Weddell Sea to South Georgia. Since 1989, they have been partially or fully occupied 14, 9 and 14 times, respectively, making them the most comprehensively sampled sections in the Weddell Sea. Most of these occupations were completed in austral summer between November and April, with occasional occupations in May and June (Methods and Supplementary Table 1). Following ref. 11, we define the WSBW as having a neutral density[33] (γ^n) denser than 28.40 kg m^{-3} and Lower WSDW as the densest AABW exported from the Weddell Sea, with a neutral density between 28.31 kg m^{-3} and 28.40 kg m^{-3}. To quantify the water-mass area, we interpolate the neutral density profiles onto a regular grid for each transect and calculate the area by summing all the grid cells falling into the relevant neutral density range of that water mass, thus accounting for the horizontal extent and layer thickness of the water mass (Extended Data Fig. 1 and Methods). A distinct decreasing trend of WSBW area is detected along all three transects, along with a concurrent decrease of Lower WSDW along the Scotia Sea part of the A23 section (Fig. 2a)[14]. Synchronous

https://doi.org/10.1038/s41558-023-01695-4

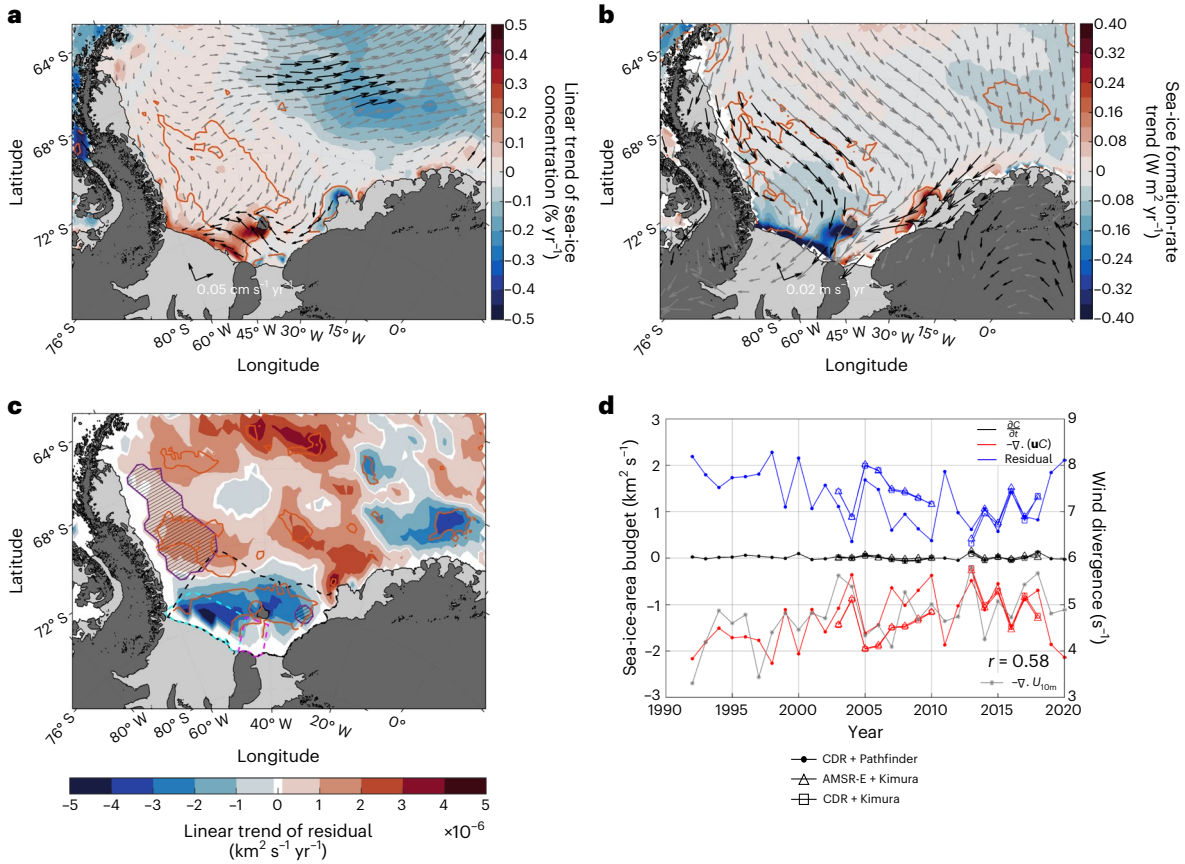

Fig. 3 | Wind-driven sea-ice formation during 1992–2020. a, Linear trend of sea-ice concentration from 1992 to 2020 estimated for austral cool season (April to October) overlaid with the ice-motion trend vectors. **b**, The sea-ice formation-rate trend but overlaid with wind-trend vectors. **c**, The linear trend of the residual (thermodynamic) term from the sea-ice-concentration budget analysis (Methods). Regions affected by mechanical redistribution are hatched and highlighted with purple (Methods). Statistical significance at 90% in sea-ice concentration, sea-ice formation-rate trend and residual term is highlighted orange contours in **a**–**c**. **d**, The area-integrated cool-season sea-ice budget terms over the southern Weddell Sea continental shelf as highlighted in **c** by black-dashed polygons. The dynamic term (red), $-\nabla\cdot(\mathbf{u}C)$, where **u** stands for the sea-ice drift velocity vector and C is the sea-ice concentration, is compensated mostly by the residual term (blue) and shows moderate correlation with the surface wind divergence (grey). An overall decreasing tendency in the residual term exists across various combinations of sea-ice concentration and sea-ice motion products. Vectors with >90% confidence in either the zonal or meridional component trend are black. Cyan and red polygons (dashed lines) along with black-dashed polygon in **c** highlight the key regions over which the sea-ice formation rate and residual term are integrated to produce the linear reduction listed in Table 1, where cyan polygon indicates Ronne Ice Shelf front and magenta polygon indicates Berkner Bank.

interannual variability is found in WSBW and Lower WSDW areas along A23 from 2012 to 2018, consistent with the connection of these dense-water-mass volumes between the Weddell Sea and Scotia Sea, in which the overflow depth on the South Scotia Ridge is a key feature controlling export volume[11,14,22]. The concurrent recovery of Lower WSDW in the Scotia Sea and Weddell Sea parts of A23 between 2016 and 2018 is likely to be associated with a short-term gyre acceleration due to anomalous wind stresses, rather than changes in source-water formation (Supplementary Fig. 1). The long-term diminution of WSBW volume accompanied by the deepening of isopycnals causes a decrease in the density of water that can overflow the South Scotia Ridge and thus be exported northwards across it.

The Weddell Sea water column consists of warm and saline WDW overlying the fresher and colder deep water masses: Upper and Lower WSDW and WSBW (Fig. 2b). The isopycnal deepening caused by WSBW contraction (Extended Data Fig. 1) can therefore lead to warming and salinification at a fixed depth via a downward displacement of warmer and saltier waters, explaining previously observed strong deep Weddell Sea warming[34]. To quantify the contribution of this process to the thermohaline trends in the Weddell Sea, we performed a water-mass property decomposition[35] (Methods) to separate the changes of temperature into changes associated with isopycnal heave and changes of temperature along isopycnals. We show that most of the deep Weddell Sea warming can be explained by heave[16,36] (Fig. 2c and Supplementary Fig. 2), which also causes a salinification trend in the deep Weddell Sea (Fig. 2d and Supplementary Fig. 3). The along-isopycnal water-mass property changes are responsible for negligible amounts of total warming across all three transects in the Weddell Sea (Supplementary Figs. 2 and 3). The full-depth warming rate (0.67 ± 0.27 W m^{-2}) in the Weddell Sea is comparable to the global ocean average (0.71 ± 0.09 W m^{-2}) (ref. 37). However, the deep Weddell Sea (>2,000 m) warming rate (0.34 ± 0.18 W m^{-2}) is found to be almost five times greater than the global average (0.07 ± 0.06 W m^{-2}) (refs. 34,37), with over 90% explained by the vertical displacement of isopycnal surfaces due to the volume reduction of WSBW (Extended Data Table 1).

Wind-forced long-term sea-ice changes

Dynamically and thermodynamically driven shifts in sea-ice concentration and formation impact the production of HSSW/DSW that feed the densest class of WSBW. On the southern Weddell Sea continental shelf, a pronounced increase in cool-season (April–October) sea-ice concentration appears around the Ronne Ice Shelf and Berkner Bank from 1992 to 2020 (Fig. 3a). Meanwhile, the bulk sea-ice formation rate[7]

https://doi.org/10.1038/s41558-023-01695-4

Table 1 | Linear reductions of sea-ice formation inferred from sea-ice formation rate and the residual term of the sea-ice concentration budget and observed and estimated WSBW-volume linear reduction

	A		B	C	D	E		F	
1	Linear reduction of sea-ice formation		Ronne+Berkner	FRIS	Linear reduction of water-mass area	AABW ($\gamma^n \geq 28.37\,kg\,m^{-3}$)		WSBW ($\gamma^n \geq 28.40\,kg\,m^{-3}$)	
2	Residual	CDR	−46.2±11.0%	−44.2±15.1%	CTD sections	A12	SR4	A12	SR4
3		BT	−46.8±11.1%	−44.0±15.3%					
4		NT	−38.2±11.4%	−40.3±15.0%	Observation	−28.6±4.4%	−20.9±3.9%	−33.0±4.8%	−34.8±4.1%
5	Sea-ice formation rate	CDR	−42.4±8.6%	−35.2±7.3%					
6		BT	−41.5±8.3%	−31.3±6.7%	Estimation	−31.8±14.3%		−59.6±86.2%	
7		NT	−35.9±6.7%	−31.5±6.7%					

All numbers are percentage reductions estimated from the linear trend of each variable from mid-July 1992 to mid-July 2020. The linear reduction of sea-ice residual term (B2–B4, C2–C4) and sea-ice formation rate (B5–B7, C5–C7) are area integrated over two regions: Ronne+Berkner, denoting the highlighted boxes seen in Fig. 3a–c with cyan and red colours, and FRIS, highlighted with the black box in Fig. 3a–c. Three sea-ice products, CDR (NOAA (National Oceanic and Atmospheric Administration)/National Snow and Ice Data Center (NSIDC) Climate Data Record of Passive Microwave Sea Ice Concentration), BT (Bootstrap Sea Ice Concentrations from Nimbus-7 Scanning Multichannel Microwave Radiometer (SMMR) and Special Sensor Microwave/Imager (SSM/I) sensors and Special Sensor Microwave Imager/Sounder (SSMIS) on the Defense Meteorological Satellite Program's (DMSP)) and NT (NASA Team Sea Ice Concentration from Nimbus-7 SMMR, and SSM/I-SSMIS on DMSP; see Methods for detailed information of sea-ice data) are used to estimate the linear reduction of sea-ice formation rate and residual terms in sea-ice budget analysis to eliminate inter-data offset. Note that the SR4 section has no available data after 2012, so a linear extrapolation is performed to obtain the linear reduction towards 2020 for the purpose of consistency. Observation (E4–E5, F4–F5) and estimation (E6–E7, F6–F7) of linear reduction of water-mass formation are estimated using two different water-mass definitions: AABW ($\gamma^n \geq 28.37\,kg\,m^{-3}$) and WSBW ($\gamma^n \geq 28.40\,kg\,m^{-3}$). The former definition represents the densest AABW components that can be exported from the Weddell Sea. Uncertainties denoted as ±1 s.d. are drawn from a Monte Carlo sampling (sample size=10^6) that is used to perform a sensitivity analysis on the estimated volume budget.

based on the sea-ice concentration, surface wind speed and air–sea temperature difference (Methods) reveals a notable decreasing trend in sensible heat loss over the front of the Ronne Ice Shelf and the northern tip of Berkner Island (Fig. 3b).These two sites are known as the main locations for HSSW production due to the persistent offshore katabatic wind and sustained coastal polynya activity[8]. The inferred reduction in sea-ice formation rate is accompanied by less sea-ice divergence and a northerly wind trend (weakened offshore wind) at the Ronne Ice Shelf and Berkner Bank that favours an increase in sea-ice concentration (Fig. 3a). The sea-ice formation rate depends strongly on sea-ice concentration in the bulk formula used; thus, a high degree of similarity between their trends is expected (Methods).

To further test the relationship between sea-ice concentration and a reduction in DSW formation, a complementary estimate of sea-ice production is obtained by conducting a sea-ice concentration-tendency analysis[38,39] using cool-season sea-ice conditions (Methods). This approach elucidates changes in sea-ice formation within the sea-ice pack, while the sea-ice formation-rate diagnostic, like other flux-based estimates[40], reflects the contribution from the changes in coastal polynya area. The dynamic term in the sea-ice-concentration budget analysis, which combines the advection and divergence of sea ice, explains the sea-ice area fluxes associated with the sea-ice drift. The residual term, being the difference between the sea-ice concentration tendency and sea-ice dynamic terms, reflects the thermodynamic melting/freezing and mechanical redistribution (ridging) of the ice[39] (Methods). The southern Weddell Sea continental shelf normally features extensive sea ice in winter and typically experiences highly divergent sea-ice motion driven by strong offshore katabatic winds. First, this means that the magnitude of sea-ice concentration tendency (the sea-ice concentration difference between two consecutive cool seasons) in this region is negligible, and therefore the residual term and dynamic sea-ice flux term compensate each other to sustain this near-zero sea-ice concentration tendency. Second, thermodynamic ice growth dominates the residual term instead of ridging (Fig. 3c and Methods). Therefore, any reduction in winter sea-ice divergence in this region will be compensated by a reduction in thermodynamic ice growth and consequent decrease in HSSW production. Over the continental shelf, the reduction of thermodynamic ice growth is pronounced at the Ronne Ice Shelf and Berkner Bank (Fig. 3c), with a broader spread over the continental shelf compared with the sea-ice formation rate, in response to a decrease in sea-ice flux divergence[41,42] that is highly correlated with wind changes ($r = 0.58$; Fig. 3d). A further decomposition of the sea-ice dynamic flux (Extended Data Fig. 2) suggests that most of the observed sea-ice flux changes are in the meridional rather than zonal direction, indicating that the wind-driven sea-ice changes are sourced mostly from the dominant meridional wind trend in the FRIS region. This suggests reduced sea-ice production within the sea-ice pack over the continental shelf beyond the coastal polynya region. The long-term trend in thermodynamic ice growth and dynamic sea-ice flux is consistent across various combinations of sea-ice-concentration and sea-ice-drift datasets (Fig. 3d).

Bottom-water loss due to sea-ice changes

A robust increase is identified in sea-ice concentration over the southern Weddell Sea continental shelf. The sea-ice concentration increase is caused by the convergent wind-driven ice-drift trends and explains the underlying declined sea-ice formation. Overall, we find a reduction in sea-ice formation of approximately 40% from 1992 to 2020 via both a bulk sea-ice formation rate estimation and a sea-ice concentration budget (Table 1). Without long-term monitoring of under-ice currents and explicit DSW volume fluxes on the continental shelf, linking the estimated reduction of sea ice to the observed diminution of WSBW on interannual timescales is challenging. Here we conduct a simple quantification to show the consistency of the two trends (Methods). We decompose the total rate of change of the bottom-water volume, dV/dt ($m^3\,s^{-1}$), into four contributing terms: two source terms (input of DSW, F, and proportionally entrained ambient water mass, E (mostly modified WDW; Extended Data Fig. 3)[42]) and two sink terms (along-isopycnal volume flux divergence, A, and diapycnal flux across the upper density bound of WSBW, D).

$$dV/dt = F + E - A - D \quad (1)$$

Volume changes of both AABW ($\gamma^n \geq 28.37\,kg\,m^{-3}$) exported from the Weddell Sea and WSBW ($\gamma^n \geq 28.40\,kg\,m^{-3}$) are assessed using the volume budget analysis and compared with observations (Table 1). We assume steady sink terms ($A + D$) and apply a reduction of the source terms to obtain a first estimate of the change in the volume budget. The volume budget deficit is then integrated over 29 years to obtain the total volume changes (Methods). Values for each term in Table 1 are derived from ref. 43 for AABW and ref. 12 for WSBW. On the basis of the preceding sea-ice analysis, an averaged 40%

https://doi.org/10.1038/s41558-023-01695-4

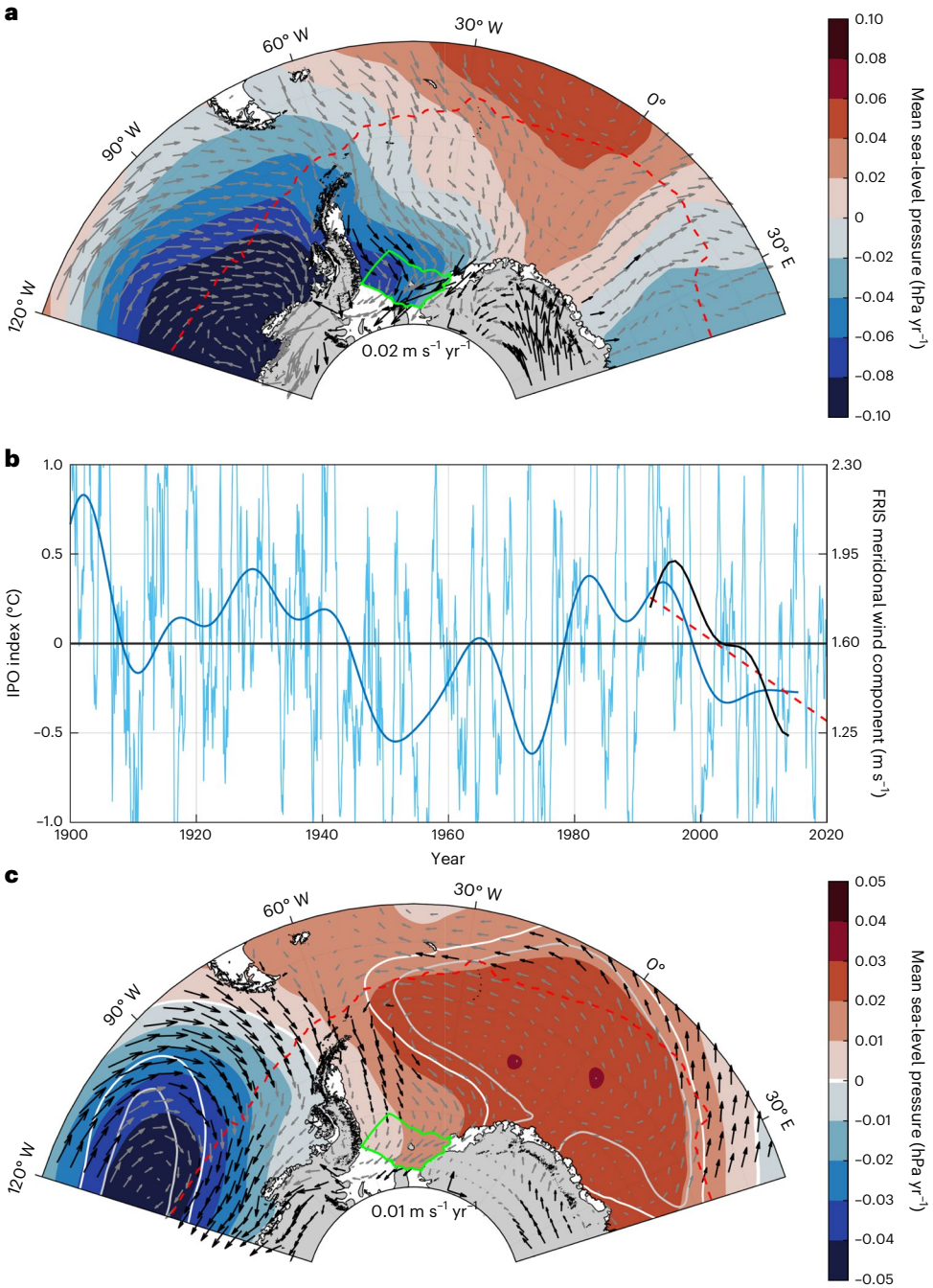

Fig. 4 | Southern Weddell Sea wind trend influenced by the IPO. a, The linear trend of cool-season-average (April–October) mean sea-level pressure and surface wind vectors from 1992 to 2020. All atmospheric fields are from the European Centre for Medium-Range Weather Forecasts Reanalysis v.5 dataset. The green polygon highlights the southern Weddell Sea continental shelf in front of the FRIS over which the meridional wind anomalies are averaged in **b**. **b**, The monthly time series of IPO overlaid (thin faded blue) with low-pass filtered IPO with a 13-year cut-off frequency (thick darker blue). A negative polarity of the IPO dominates the period since 1992 (red), accompanied by weakened meridional wind in the FRIS (black line). **c**, The trend of cool-season-averaged (April–October) mean sea-level pressure and surface wind vectors associated with the negative polarity of IPO over the period from 1992 to 2020. The fields in **c** are produced using cool-season-averaged interannual wind, mean sea-level pressure and IPO index. Regressions of wind and mean sea-level pressure onto the IPO index are multiplied by the linear trend of IPO since 1992. The 90% confidence level of mean sea-level pressure trend and surface wind vector trend is indicated by white contours and black arrows in **a** and **c**.

reduction is applied to the bottom-water source terms ($F + E$) for both water-mass evaluations, yielding a 31.8 ± 14.3% AABW reduction and 59.6 ± 86.2% WSBW reduction over the 29 years (Methods). We note that this calculation assumes a constant along-isopycnal flux out of the Weddell Sea, A, which is expected to decline over time due to the thinning of the isopycnal layers bounding the target water masses. Therefore, our estimated values probably mark the upper bound of the bottom-water volume reduction. The estimated WSBW reduction has a large uncertainty, which derives from the comparable magnitude of volume transport errors estimated by ref. 12 where the advection and diapycnal mixing terms themselves are not well constrained (Methods). Nevertheless, within uncertainty, our estimated values can account

for the 20–30% reduction of AABW/WSBW volume across A12 and SR4, suggesting the observed sea-ice changes alone are sufficient to explain the observed WSBW reduction. Our calculation supports the proposed link between the wind-driven sea-ice formation changes and the observed AABW/WSBW volume reduction that fits both the observational data and the existing physical understanding. This new chain of causation will be further investigated in the future following the development of suitable models.

Climatic dependence of FRIS winds

A widespread Amundsen Sea Low (ASL) deepening[38] and an increase in mean sea-level pressure to the east of the Weddell Sea are observed in the reanalysis mean sea-level pressure-trend map (Fig. 4a). This trend in the zonal pressure gradient sustains the observed northerly wind trend over the Southern Weddell Sea (Fig. 4a). The ASL deepening is known as a response to sea-level pressure anomalies excited by tropical Pacific sea surface temperature variability, which propagates towards the ASL region via an atmospheric Rossby wave train[44,45]. We show that a transition of positive IPO into its negative phase since 1992 (Fig. 4b) is concurrent with the northerly wind trend (Fig. 4b). The observed atmospheric trends (Fig. 4a) can be reproduced to a notable extent with the linear regressions of mean sea-level pressure and wind vectors onto the IPO index multiplied by the linear trend of IPO estimated from 1992 to 2020 (Fig. 4c). The ASL deepening in recent decades has also been related to a positive trend in the Atlantic Multidecadal Oscillation[45]. However, our linear regression analysis demonstrates that although this trend does produce an ASL deepening trend, it does not reproduce the zonal gradients over the southern Weddell Sea necessary for a northerly FRIS meridional wind trend (Extended Data Fig. 4).

Inevitably, the total FRIS wind trend cannot be attributed solely to the IPO index. Only 24% of the FRIS wind trend can be retrieved from the linear regression, and less than 10% of the total observed wind variance, with most of the variability left in the residual term from the linear regression model (Extended Data Fig. 5). The reconstructed wind (Extended Data Fig. 5) can explain up to 30% of the total wind trend if the influence of the Southern Annular Mode (SAM) is also considered. Conversely, the FRIS meridional wind correlates well with ASL longitude ($r = -0.56$, $P < 0.01$; Extended Data Fig. 6), a metric reflecting not just ASL position but also zonal sea-level pressure-trend gradients over the Weddell Sea that are relevant for FRIS wind changes. The fluctuation of ASL position could be associated with the interaction between planetary waves and local topography[46]. However, there is no significant trend in the position of the ASL, meaning this may drive interannual variability but cannot be positively attributed as a cause for the observed trends in sea-ice concentration. These results highlight the sensitivity of FRIS wind to the intrinsic fluctuation of the ASL system, while the complex interplay between remote climatic modes and local systems challenges the attribution of Weddell Sea wind trend and shorter-term variability. Further work will focus on further decoupling the local and remote drivers and mechanisms of FRIS wind variability.

Discussion

Recently, the IPCC report assessed that AABW formation will decline in a warming world due to the increased stratification associated with freshwater input from the Antarctic Ice Sheet[47]. Such a long-term trend can be episodically disrupted by enhanced sea-ice formation that (over-)compensates the impact of ice-sheet melting, causing enhanced AABW formation in the Ross[48] and Weddell seas[7]. Our results show that, over the observational record, this does not hold within the Weddell Sea, and instead, wind-driven sea-ice changes emerge as the key regulator of the AABW formation trends in the Weddell Sea.

These sea-ice changes and the resultant sea-ice production trend within coastal polynyas and over the continental shelf are found to be dominated by the changes in the surface wind and its divergence. These signals are also coincident with the negative polarity of the IPO (Extended Data Fig. 7), although it is not possible at present to attribute the majority of the trend to this driver (Extended Data Fig. 5). The Weddell Sea wind variability on shorter timescales is tentatively associated with the internal variability of the ASL system (Extended Data Fig. 6). These results highlight the importance of understanding the response of Weddell Sea wind to remote climate variability and the role of natural variability in multidecadal trends in subpolar circulation to evaluate this potential near-planetary-scale teleconnection between the tropical Pacific and abyssal Atlantic. Although the FRIS meridional wind variability and part of its trend are attributed to natural variability, the cool-season SAM index elevates the predicted FRIS wind trend such that the combination of SAM and IPO represents a greater fraction of FRIS wind trend than the IPO index alone (Extended Data Fig. 5). Considering that this 'improvement' in reconstructed wind trend is relatively small (<10%) and that the cool-season SAM trend over the period of interest can be affected by both the internal variability and external forcing[49], there is no clear evidence so far suggesting that the external forcing plays a leading role driving the observed FRIS wind trend and variability over the past three decades. However, the sign of these recent wind trends is consistent with that expected from the wind response to high greenhouse gas emission scenarios in coupled climate models[50], indicating that the WSBW volume contraction may continue under such scenarios regardless of natural variability.

Our study proposes a link between wind-driven sea-ice changes and WSBW volume reduction that is supported by the existing observational evidence and bottom-water formation theory. Future work is needed to develop and explore a suitable model consisting of ocean, sea-ice and ice-shelf components and representing dense-water cascading and other fine-scale processes governing the mixing on the continental slope, so as to further confirm the causal relation between surface wind and the WSBW reservoir. More important, to confidently address the AABW changes in climate models in the future, the interplays among ocean, ice and atmosphere, and especially sea-ice formation in response to climatic modes, need to be resolved to better understand the response of the abyssal ocean heat/carbon storage to climate change.

Online content

Any methods, additional references, Nature Portfolio reporting summaries, source data, extended data, supplementary information, acknowledgements, peer review information; details of author contributions and competing interests; and statements of data and code availability are available at https://doi.org/10.1038/s41558-023-01695-4.

References

1. Johnson, G. C. Quantifying Antarctic Bottom Water and North Atlantic Deep Water volumes. *J. Geophys. Res.* **113**, C05027 (2008).
2. Lumpkin, R. & Speer, K. Global ocean meridional overturning. *J. Phys. Oceanogr.* **37**, 2550–2562 (2007).
3. Ferrari, R. et al. Antarctic sea ice control on ocean circulation in present and glacial climates. *Proc. Natl Acad. Sci. USA* **111**, 8753–8758 (2014).
4. Orsi, A. H., Johnson, G. C. & Bullister, J. L. Circulation, mixing, and production of Antarctic Bottom Water. *Progr. Oceanogr.* **43**, 55–109 (1999).
5. Meredith, M. P. Replenishing the abyss. *Nat. Geosci.* **6**, 166–167 (2013).
6. Janout, M. A. et al. FRIS revisited in 2018: on the circulation and water masses at the Filchner and Ronne ice shelves in the southern Weddell Sea. *J. Geophys. Res. Oceans* **126**, e2021JC017269 (2021).

7. Hattermann, T. et al. Observed interannual changes beneath Filchner–Ronne Ice Shelf linked to large-scale atmospheric circulation. *Nat. Commun.* **12**, 2961 (2021).
8. Nicholls, K. W., Østerhus, S., Makinson, K., Gammelsrød, T. & Fahrbach, E. Ice–ocean processes over the continental shelf of the southern Weddell Sea, Antarctica: a review. *Rev. Geophys.* **47**, RG3003 (2009).
9. Weppering, R. Isotope data from Ice Station Weddell: implications for deep water formation in the Weddell Sea. *J. Geophys. Res.* **101**, 25723–25739 (1996).
10. Darelius, E. & Sallée, J.-B. Seasonal outflow of ice shelf water across the front of the Filchner Ice Shelf, Weddell Sea, Antarctica. *Geophys. Res. Lett.* **45**, 3577–3585 (2018).
11. Meredith, M. P., Naveira-Garabato, A. C., Gordon, A. L. & Johnson, G. C. Evolution of the deep and bottom waters of the Scotia Sea, Southern Ocean, during 1995–2005. *J. Clim.* **21**, 3327–3343 (2008).
12. Jullion, L. et al. The contribution of the Weddell Gyre to the lower limb of the global overturning circulation. *Geophys. Res. Lett.* **119**, 3357–3377 (2014).
13. Naveira-Garabato, A. C. et al. The thermodynamic balance of the Weddell Gyre. *Geophys. Res. Lett.* **43**, 317–325 (2016).
14. Abrahamsen, E. P. et al. Stabilization of dense Antarctic water supply to the Atlantic Ocean overturning circulation. *Nat. Clim. Change* **9**, 742–746 (2019).
15. Rintoul, S. R. Rapid freshening of Antarctic Bottom Water formed in the Indian and Pacific oceans. *Geophys. Res. Lett.* **34**, L06606 (2007).
16. Purkey, S. G. & Johnson, G. C. Antarctic Bottom Water warming and freshening: contributions to sea level rise, ocean freshwater budgets, and global heat gain. *J. Clim.* **26**, 6105–5122 (2013).
17. Bindoff, N. & Hobbs, W. Deep ocean freshening. *Nat. Clim. Change* **3**, 864–865 (2013).
18. Menezes, V. V., McDonald, A. M. & Schatzman, C. Accelerated freshening of Antarctic Bottom Water over the last decade in the southern Indian Ocean. *Sci. Adv.* **3**, e1601426 (2017).
19. Shepherd, A., Wingham, D. & Rignot, E. Warm ocean is eroding West Antarctic Ice Sheet. *Geophys. Res. Lett.* **31**, L23402 (2004).
20. Jacobs, S. S., Giulivi, C. F. & Dutrieux, P. Persistent Ross Sea freshening from imbalance West Antarctic Ice Shelf melting. *J. Geophys. Res. Oceans* **127**, e2021JC017808 (2022).
21. Jullion, L. et al. Decadal freshening of the Antarctic Bottom Water exported from the Weddell Sea. *J. Clim.* **26**, 8111–8125 (2013).
22. Meredith, M. P. et al. Synchronous intensification and warming of Antarctic Bottom Water outflow from the Weddell Gyre. *Geophys. Res. Lett.* **38**, L03603 (2011).
23. Darelius, E., Fer, I. & Nicholls, K. Observed vulnerability of Filchner–Ronne Ice Shelf to wind-driven inflow of warm deep water. *Nat. Commun.* **7**, 12300 (2016).
24. Hellmer, H. H., Kauker, F., Timmermann, R., Determann, J. & Rae, J. Twenty-first-century warming of a large Antarctic ice-shelf cavity by a redirected coastal current. *Nature* **485**, 225–228 (2012).
25. Naughten, K. A. et al. Two-timescale response of a large Antarctic ice shelf to climate change. *Nat. Commun.* **12**, 1991 (2021).
26. Siahaan, A. et al. The Antarctic contribution to 21st-century sea-level rise predicted by the UK Earth System Model with an interactive ice sheet. *Cryosphere* **16**, 4053–4086 (2022).
27. Rignot, E., Jacobs, S. S., Mouginot, J. & Scheuchl, B. Ice-shelf melting around Antarctica. *Science* **341**, 266–270 (2013).
28. Paolo, F. S., Fricker, H. A. & Padman, L. Volume loss from Antarctic ice shelves is accelerating. *Science* **348**, 327–331 (2015).
29. Power, S., Casey, T., Folland, C., Colman, A. & Mehta, V. Inter-decadal modulation of the impact of ENSO on Australia. *Clim. Dyn.* **15**, 319–324 (1999).
30. Meehl, G. A., Arblaster, J. M., Bitz, C. M., Chung, C. T. Y. & Teng, H. Antarctic sea-ice expansion between 2000 and 2014 driven by tropical Pacific decadal climate variability. *Nat. Geosci.* **9**, 590–595 (2016).
31. Purich, A. et al. Tropical Pacific SST drivers of recent Antarctic sea ice trends. *J. Clim.* **29**, 8931–8948 (2016).
32. Schneider, D. P. & Deser, C. Tropically driven and externally forced patterns of Antarctic sea ice change: reconciling observed and modeled trends. *Clim. Dyn.* **50**, 4599–4618 (2018).
33. Jackett, D. R. & McDougall, T. J. A neutral density variable for the world's oceans. *J. Phys. Oceanogr.* **27**, 237–263 (1997).
34. Strass, V. H., Rohardt, G., Kanzow, T., Hoppema, M. & Boebel, O. Multidecadal warming and density loss in the deep Weddell Sea, Antarctica. *J. Clim.* **33**, 9863–9881 (2020).
35. Bindoff, N. L. & McDougall, T. J. Diagnosing climate change and ocean ventilation using hydrographic data. *J. Phys. Oceanogr.* **24**, 1137–1152 (1994).
36. Purkey, S. G. & Johnson, G. C. Global contraction of Antarctic Bottom Water between the 1980s and 2000s. *J. Clim.* **25**, 5830–5844 (2012).
37. Desbruyères, D., McDonagh, E. L., King, B. A. & Thierry, V. Global and full-depth ocean temperature trends during the early twenty-first century from Argo and repeat hydrography. *J. Clim.* **30**, 1985–1997 (2017).
38. Holland, P. R. & Kwok, R. Wind-driven trends in Antarctic sea-ice drift. *Nat. Geosci.* **5**, 872–875 (2012).
39. Holland, P. R. & Kimura, N. Observed concentration budgets of Arctic and Antarctic sea ice. *J. Clim.* **29**, 5241–5249 (2016).
40. Tamura, T., Oshima, K. I., Fraser, A. D. & William, G. D. Sea ice production variability in Antarctic coastal polynyas. *J. Geophys. Res. Oceans* **121**, 2967–2979 (2016).
41. Drucker, R., Seeley, M. & Kwok, R. Sea ice production and export from coastal polynyas in the Weddell and Ross seas. *Geophys. Res. Lett.* **38**, L17502 (2011).
42. Kwok, R., Pang, S. S. & Kacimi, S. Sea ice drift in the Southern Ocean: regional patterns, variability, and trends. *Elementa* https://doi.org/10.1525/elementa.226 (2017).
43. Akhoudas, C. A. et al. Ventilation of the abyss in the Atlantic sector of the Southern Ocean. *Sci. Rep.* **11**, 6760 (2021).
44. Karoly, D. J., Plumb, R. A. & Ting, M. Examples of horizontal propagation of quasi-stationary waves. *J. Atmos. Sci.* **46**, 2802–2811 (1989).
45. Li, X. et al. Tropical teleconnection impacts on Antarctic climate changes. *Nat. Rev. Earth Environ.* **2**, 680–698 (2021).
46. Lachlan-Cope, T. A., Connolley, W. M. & Turner, J. The role of the non-axisymmetric Antarctic orography in forcing the observed pattern of variability of the Antarctic climate. *Geophys. Res. Lett.* **28**, 4111–4114 (2001).
47. Fox-Kemper, B. et al. in *Climate Change 2021: The Physical Science Basis* (eds Masson-Delmotte, V. et al.) 1211–1362 (Cambridge Univ. Press, 2021).
48. Silvano, A. et al. Recent recovery of Antarctic Bottom Water formation in the Ross Sea driven by climate anomalies. *Nat. Geosci.* **13**, 780–786 (2020).
49. Fogt, R. L. & Marshall, G. The Southern Annular Mode: variability, trends, and climate impacts across the Southern Hemisphere. *Wiley Interdiscip. Rev. Clim. Change* **11**, e652 (2020).
50. Neme, J., England, M. H. & Hogg, A. M. C. Projected changes of surface winds over the Antarctic continental margin. *Geophys. Res. Lett.* **49**, e2022GL098820 (2022).

Methods

Water-mass area computation

WSBW areas are computed along hydrographic transects following ref. 14. We used three hydrographic sections, A23, SR4 and A12, to compile the AABW/WSBW changes. In total, we used 14 A23 (64° S–55° S) occupations from 1995 to 2021, 9 SR4 occupations from 1989 to 2013 and 14 A12 occupations from 1992 to 2019 (Supplementary Table 1). Briefly, a consistent transect line is selected on the basis of the most complete occupation for each transect. The horizontal coordinates are calculated by finding the sampling-station position along each transect line. The grid has a horizontal resolution of 1 km and a vertical resolution of 2 m. Profile data are extrapolated vertically from the first and last measurements to the surface and bottom if necessary. The depth mask, based on ref. 51 (v.20.1, February 2020) is applied to determine the bottom for each interpolated station. Neutral densities (γ^n) (ref. 33) are computed for each profile using Matlab routine of eos80_legacy_gamma_n of ref. 33 and then linearly interpolated (horizontally and vertically) onto the grid, with profile data extrapolated in the vertical to the surface or bottom if necessary. The number of grid cells that fall in each density range is summed and multiplied by the grid-cell area to obtain the water-mass area. The WSBW is defined as water mass with γ^n denser than 28.40 kg m^{-3}. The densest water mass within AABW exported from Weddell Sea, Lower WSDW, spills over the abyssal Scotia Sea with characteristic γ^n denser than 28.31 kg m^{-3}. The error bars of water-mass area in Fig. 2 are computed by combining the instrumental uncertainties of temperature and salinity measurements, ±0.001 °C and ±0.002, respectively. The magnitude of the upper bound displayed in Fig. 2a marks the water-mass area estimated using γ^n computed with all the temperature measurements being lowered by 0.001 °C and salinity measurements being increased by 0.002 to account for the most overestimated γ^n fields due to instrumental errors. Likewise, the lower bound of water-mass area is derived from the γ^n fields computed with all the temperature measurements being increased by 0.001 °C and salinity measurements being lowered by 0.002. The resultant uncertainties from temperature and salinity perturbations are approximately symmetric around zero[14]. The error bars do not mask the overall decreasing trend of WSBW area displayed in Fig. 2a.

Temperature and salinity trend decomposition

Conservative temperature (Θ) and absolute salinity (S_A) are computed using the Gibbs-Sea Water oceanographic toolbox containing the Thermodynamics Equation of Seawater (TEOS-10) subroutines[52] for each profile. Profile data are then interpolated onto the same transect grid created for water-mass area calculation. This creates a continuous temperature and salinity at the same transect grid point. We retain the missing data to avoid false signals near the bottom and slope. The decomposition scheme follows the principle described by ref. 35,

$$\frac{\mathrm{d}\Theta}{\mathrm{d}t}|_P \simeq \frac{\mathrm{d}\Theta}{\mathrm{d}t}|_{\gamma^n} - \frac{\mathrm{d}P}{\mathrm{d}t}|_{\gamma^n}\overline{\frac{\partial\Theta}{\partial P}}$$

$$\frac{\mathrm{d}S_A}{\mathrm{d}t}|_P \simeq \frac{\mathrm{d}S_A}{\mathrm{d}t}|_{\gamma^n} - \frac{\mathrm{d}P}{\mathrm{d}t}|_{\gamma^n}\overline{\frac{\partial S_A}{\partial P}}$$

This decomposition separates the total temperature and salinity variability into the contribution from adiabatic isopycnal heaving associated with dynamical variability and diabatic water-mass property changes along isopycnal surface. We retain the missing data when interpolating profile data onto the transect grid, and only grid points containing over 50% valid data are shown in the trend map to ensure that the signals seen are robust. Note that the computation of the isopycnal heaving component adopts a linearization of background stratification, and only the time-mean stratification is used. This practice inevitably introduces errors in the results, that is, discrepancies between the sum of decomposed components and observed total temperature/salinity trend at a given pressure level, especially in the region where the vertical gradient of temperature and salinity is large (in thermocline and halocline)[53]. The intermittent diapycnal mixing near the bottom of the ocean also increases the residual magnitude (Supplementary Fig. 4a,b). One way to reduce this is to represent the isopycnal heaving component as a residual between total temperature/salinity variability observed at a pressure level and the along-isopycnal changes[54,55]. Using this approach, the resultant heaving component still accounts for the majority of the observed deep warming and salinification (Supplementary Fig. 4c,d).

Sea-ice formation rate

Sea-ice formation rates (SFRs) are estimated following a bulk formula[7] that essentially computes the available sensible heat loss at a given sea-ice concentration (SIC), $\mathrm{SFR} = \rho^{\mathrm{air}} c_p^{\mathrm{air}} C_s\,(1 - \mathrm{SIC})\,U\Delta T$. Constant parameters in the formula are density of air, $\rho^{\mathrm{air}} = 1.3$ kg m^{-3}, specific heat capacity, $c_p^{\mathrm{air}} = 1{,}000$ J kg^{-1} K^{-1} and sensible heat transfer coefficient, $C_s = 1.5 \times 10^{-3}$. The temperature difference between the ocean surface freezing point and 2 m air temperature is given as $\Delta T = -1.9 - T^{\mathrm{air}}$. The surface wind speed U and air temperature T^{air} come from the ERA5 reanalysis dataset, with a 31 km horizontal resolution and daily temporal resolution. Three sea-ice concentration products (Table 1), NOAA/NSIDC Climate Data Record of Passive Microwave Sea Ice Concentration (CDR[56]), Sea Ice Concentration from DMSP SSM/I-SSMIS Passive Microwave Data using NASA Team (NT) algorithm (v.1.0[57]) and Sea Ice Concentration from DMSP SSM/I-SSMIS using Bootstrap (BT) algorithm (v.3.0[58]) are used to eliminate inter-data bias. Only data after 1992 are selected for estimation for the consistency in sensors and orbit coverage. The sea-ice formation rate time series is predominantly a function of sea-ice concentration. The sea-ice concentration dominates the sea-ice formation-rate trend and variability. Both the wind speed and surface air temperature contributed only a limited fraction of trend to the sea-ice formation rate and only weakly correlated with the sea-ice formation rate (Supplementary Tables 2 and 3), consistent with the findings by ref. 7.

Sea-ice concentration-tendency analysis and sea-ice drift data

The sea-ice budget analysis is performed following ref. 39 using daily sea-ice concentration and sea-ice drift data. In this study, we used four sea-ice concentration datasets, CDR, NT, BT and sea-ice concentration derived from 12.5 km Advanced Microwave Scanning Radiometer for Earth Observing Satellite (AMSR-E) brightness temperature[59], and two sea-ice drift datasets (Pathfinder[60] and Kimura[61]) to valid our interpretation on the estimated sea-ice formation. CDR and AMSR-E are cross-paired with Pathfinder and Kimura drift to address the bias between sea-ice drift products. We found that the choice of sea-ice drift products does not qualitatively change the observed interannual variability in sea-ice budget terms. Due to the data gap in AMSR-E sea-ice concentration and Kimura drift, we therefore use the continuous CDR (as well as NT and BT) sea-ice concentration and Pathfinder sea-ice drift to estimate the long-term trend in sea-ice budget analysis terms. CDR, NT and BT sea-ice concentration data are further paired with Pathfinder to eliminate inter-data bias from sea-ice algorithms (Table 1).

In each sea-ice concentration and sea-ice drift pair, sea-ice concentration data are first binned into the sea-ice drift grid (Equal-Area Scalable Earth 25 km grid v.2.0[62] for Pathfinder drift and a native 60 km polar stereographic grid for Kimura drift) to compute the sea-ice advection and divergence terms,

$$\frac{\partial C}{\partial t} = -\nabla \cdot (\mathbf{u}C) + \text{residual}.$$

The sea-ice concentration tendency, $\frac{\partial C}{\partial t}$, for each day is computed as a central difference in time from sea-ice concentration, C, fields from the day before and day after. The advection and divergence, $-\nabla \cdot (\mathbf{u}C)$,

are computed as a central difference in space and then averaged over the same three-day period to obtain a consistent time stamp, where **u** stands for the sea-ice drift vector. The residual term therefore reflects the thermodynamic response of sea ice to the dynamic sea-ice fluxes. One exceptional scenario where the residual term does not reflect the thermodynamic changes of sea ice is when the sea ice are colliding with each other over the region with high sea-ice concentration. In this case, the sea-ice concentration is saturated with near-zero sea-ice concentration tendency, whereas the sea-ice divergence is negative (convergence), which needs to be compensated by a positive residual term. The positive residual term here, therefore, does not reflect the increase in sea-ice formation. This sea-ice ridging effect may dominate only when the averaged residual is negative (a sea-ice concentration sink), averaged sea-ice drift is convergent and averaged sea-ice concentration is high (>80%). In the region of the southern Weddell Sea continental shelf, sea-ice flux is highly divergent, and the thermodynamic ice growth dominates the residual term (Fig. 3c). In this study, we tried various combinations of sea-ice concentration and sea-ice drift pairs to perform the sea-ice budget analysis. The trend map shown in Fig. 3c is the results computed from daily CDR[56] sea-ice concentration and daily Pathfinder 25 km ice drift v.4[60]. A summary of the linear reduction in the residual term obtained from Pathfinder drift and two other continuous sea-ice concentration datasets—NT and BT—can be found in Table 1. Trends are qualitatively the same with a better match between BT and CDR. We also show the time series of the sea-ice budget term integrated over the southern Weddell Sea continental shelf computed from two other sea-ice concentration + drift pairs—AMSR-E + Kimura drift[61]an CDR + Kimura drift—to assess the impact of the sea-ice drift data choice. The sea-ice drift imposes a small difference on budget terms but does not alter the overall decreasing trend in residual and converging sea-ice tendency in the FRIS region.

Bottom-water-volume budget analysis

In the bottom-water-volume budget analysis, we compute the estimated bottom-water volume reduction using equation (1) as follows,

$$\mathrm{d}V/\mathrm{d}t = F + E - A - D$$

The volume changes rate $\mathrm{d}V/\mathrm{d}t$ on the left-hand side of the equation is assumed to be zero initially as we assume the mean state/climatological condition of the bottom-water volume; that is, the terms on the right-hand side—F (DSW input), E (modified WDW entrainment), A (bottom-water advection along isopycnal) and D (bottom-water consumption via diapycnal mixing)—are in equilibrium with each other. We obtain these initial balanced values for each term for WSBW and AABW from two studies, respectively, ref. 12 and ref. 43. The initial value for each term comes with a mean value (considered as its climatological mean) and an uncertainty provided by the relevant study (± certain value). For the WSBW case, ref. 12 gave the explicit estimates of WSBW advection ($\gamma^n \geq 28.40$ kg m^{-3}) and diapycnal mixing ($A + D = -4 \pm 2$ Sv, 1 Sv = 1×10^6 m^3 s^{-1}) but no estimate for $F + E$. Since we are assuming F, E, A and D are balanced with each other and $\mathrm{d}V/\mathrm{d}t$ is zero initially, we can assume $F + E = 4 \pm 2$ Sv. For AABW, ref. 43 applied a linear mixing framework on the Weddell Sea-origin AABW with a targeted density range $\gamma^n \geq 28.37$ kg m^{-3}. In total, 4.5 ± 0.3 Sv DSW (F) and 3.9 ± 0.5 Sv modified WDW (E) contributed to the net 8.4 ± 0.7 Sv AABW production, balanced by the sinking terms ($A + D = -8.4 \pm 0.7$ Sv). Among the total 4.5 Sv DSW input, 3 ± 0.6 Sv comprised newly ventilated at Southern Weddell Sea continental shelf, F_{southern}, and a corresponding 2.6 ± 0.6 Sv modified WDW was entrained into this portion of cascading DSW plumes, E_{southern}, assuming the ratio of DSW to modified WDW of AABW as identified in ref. 43 using tracer fingerprints is conserved. To estimate the combined uncertainty of this relationship, we used a Monte Carlo model, where we iteratively perturbed all terms from their climatological mean within the range of their own uncertainties, independently. In each iteration, after terms are perturbed, a 40% reduction is then applied only on the source term ($F + E$) to obtain the amount of resultant volume-change rate $\mathrm{d}V/\mathrm{d}t$ due to the observed reduction in sea-ice formation. Note that for AABW, the 40% reduction is applied only to $F_{\mathrm{southern}} + E_{\mathrm{southern}}$. We integrate the subsequent volume-change rate ($\mathrm{d}V/\mathrm{d}t$) over 29 years (1992–2020) to obtain the total volume change ($\mathrm{d}V$). The linear reduction percentage is obtained by dividing the integral volume change by the climatological volume of WSBW (2.47×10^{15} m^3) and AABW (5.69×10^{15} m^3) estimated using a neutral density climatology computed from the World Ocean Atlas 2018. The Monte Carlo is iterated for 1,000,000 times for both WSBW and AABW cases to obtain an ensemble of volume changes of WSBW and AABW caused by 40% reduction of DSW production, which allows us to calculate the mean volume change and uncertainty.

The assumption of fixed advection in our estimation may lead to an underestimate of the overall reduction. This is because the reduction of WSBW volume is accompanied by a deepening of density surfaces and consequently a smaller area of advective flux out of the Weddell Sea volume. Assuming constant velocities, this will lead to a reduction in export roughly proportional to the change in area. This would also be consistent with reduced AABW volumes observed north of the Weddell Sea[36,63].

Changes in diapycnal mixing could also affect the volume of WSBW once it has been formed and resides in the Weddell Sea reservoir. Such changes are not readily quantifiable using available data; here this term is taken to be constant. The effectiveness of the diapycnal mixing in the deep ocean that transforms cold DSW into AABW depends on the internal wave breaking associated with the turbulence over topography and water-mass exchange between boundary current and ocean interior[64]. Eddy kinetic energy (EKE) inferred from sea-ice corrected altimetry data[65–67] can be suggestive for the evolution of the mixing triggered by such internal wave breaking within the gyre domain. Here we combine two altimetry data products—10 yr Envisat-RA2 (2002–2012) and 10 yr Cryosat-2 (2010-2020)—to assess EKE evolution from 2002 to 2020. In the Weddell Sea, EKE fluctuates mostly within the boundary current, whereas the gyre interior is less dynamic (Supplementary Fig. 5a). Within the open ocean of the Weddell Domain, there is no significant EKE trend (Supplementary Fig. 5b), suggesting that there is possibly no elevated mixing triggered by internal wave activity/breaking. The weak diapycnal mixing changes is also supported by small residuals in the deep ocean temperature and salinity trend decomposition (Supplementary Fig. 4a,b). Therefore, for our purpose, a constant diapycnal contribution of volume transport inferred from the inverse method is perhaps the most conservative approach.

Data availability

All the ship–CTD data are available from the British Oceanographic Data Centre (https://www.bodc.ac.uk/), Pangaea Data Publisher (https://www.pangaea.de/)[68–84] and CLIVAR and Carbon Hydrographic Data Office (https://cchdo.ucsd.edu/). Links to the data are available in Supplementary Table 1. Sea-ice concentration and Pathfinder sea-ice drift data are publicly accessible from the National Snow & Ice Data Center (https://nsidc.org/). ERA5 reanalysis data are archived in the Climate Data Store (https://cds.climate.copernicus.eu/). The IPO index is available from NOAA Physical Sciences Laboratory (https://psl.noaa.gov/data/timeseries/IPOTPI/). The monthly, observational-based SAM index is used in this study, and it is available from https://legacy.bas.ac.uk/met/gjma/sam.html. The AMO index is available from NOAA Physical Sciences Laboratory (https://legacy.bas.ac.uk/met/gjma/sam.html). The topography and coastline data used in Fig. 1 are from RTopo-2 dataset, available at Pangaea Data Publisher (https://doi.org/10.1594/PANGAEA.856844)[85]. The water-mass-area time-series data used to produce Fig. 2a are available at Figshare (https://doi.org/10.6084/m9.figshare.22718794)[86].

Code availability

Scripts used to compute water-mass area in this study are available at the Zenodo repository (https://doi.org/10.5281/zenodo.7919319)[87]. Scripts used to perform sea-ice-concentration-tendency analysis are available at the Zenodo repository (https://doi.org/10.5281/zenodo.7919315)[88].

References

51. Smith, W. H. F. & Sandwell, D. T. Global sea floor topography from satellite altimetry and ship depth soundings. *Science* **277**, 1956–1962, https://doi.org/10.1126/science.277.5334.1956 (1997).
52. McDougall T. J. & Barker, P. M. *Getting Started with TEOS-10 and the Gibbs Seawater (GSW) Oceanographic Toolbox* http://www.teos-10.org/publications.htm (SCOR/IAPSO WG127, 2011).
53. Desbruyères, D. et al. Full-depth temperature trends in the northeastern Atlantic through the early 21st century. *Geophys. Res. Lett.* **41**, 7971–7979 (2014).
54. Doney, S. C., Yeager, S., Danabasoglu, G., Large, W. G. & McWilliams, J. C. Mechanisms governing interannual variability of upper-ocean temperature in a global ocean hindcast simulation. *J. Phys. Oceanogr.* **37**, 1918–1938 (2007).
55. Clément, L., McDonagh, E. L., Marzocchi, A. & Nurser, A. J. G. Signature of ocean warming at the mixed layer base. *Geophys. Res. Lett.* **47**, e2019GL086269 (2019).
56. Meier, W. N., Fetterer, F., Windnagel, A. K. & Stewart, S. *NOAA/NSIDC Climate Data Record of Passive Microwave Sea Ice Concentration, Version 4*; https://doi.org/10.7265/efmz-2t65 (NSIDC, 2021).
57. Cavalieri, D. J., Parkinson, C. L., Gloersen, P. & Zwally., H. J. *Sea Ice Concentrations from Nimbus-7 SMMR and DMSP SSM/I-SSMIS Passive Microwave Data, Version 1* https://doi.org/10.5067/8GQ8LZQVL0VL (NSIDC, 1996).
58. Comiso, J. C. *Bootstrap Sea Ice Concentrations from Nimbus-7 SMMR and DMSP SSM/I-SSMIS, Version 3* https://doi.org/10.5067/7Q8HCCWS4I0R (NSIDC, 2017).
59. Cavalieri, D. J., Markus, T. & Comiso, J. C. *AMSR-E/Aqua Daily L3 12.5 km Brightness Temperature, Sea Ice Concentration, and Snow Depth Polar Grids, Version 3* https://doi.org/10.5067/AMSR-E/AE_SI12.003 (NSIDC, 2014).
60. Tschudi, M., Meier, W. N., Stewart, J. S., Fowler, C. & Maslanik, J. *Polar Pathfinder Daily 25 km EASE-Grid Sea Ice Motion Vectors, Version 4* https://doi.org/10.5067/INAWUWO7QH7B (NSIDC, 2019).
61. Kimura, N., Nishimura, A., Tanaka, Y. & Yamaguchi, H. Influence of winter sea-ice motion on summer ice cover in the Arctic. *Polar Res.* **32**, 20193 (2013).
62. Brodzik, M. J., Billingsley, B., Haran, T., Raup, B. & Savoie, M. H. EASE-Grid 2.0: incremental but significant improvements for Earth-gridded data sets. *ISPRS Int. J. Geoinf.* **1**, 32–45 (2012).
63. Campos, E. J. D. et al. Warming trend in Antarctic Bottom Water in the Vema Channel in the South Atlantic. *Geophys. Res. Lett.* **48**, e2021GL094709 (2021).
64. Naveira-Garabato, A. C. et al. Rapid mixing and exchange of deep-ocean waters in an abyssal boundary current. *Proc. Natl Acad. Sci. USA* **116**, 13233–13238 (2019).
65. Armitage, T. W. K., Kwok, R., Thompson, A. F. & Cunningham, G. Dynamic topography and sea level anomalies of the Southern Ocean: variability and teleconnections. *J. Geophys. Res. Oceans* **123**, 613–630 (2018).
66. Dotto, T. S. et al. Variability of the Ross Gyre, Southern Ocean: drivers and responses revealed by satellite altimetry. *Geophys. Res. Lett.* **45**, 6195–6204 (2018).
67. Naveira-Garabato, A. C. et al. Phased response of the subpolar Southern Ocean to changes in circumpolar winds. *Geophys. Res. Lett.* **46**, 6024–6033 (2019).
68. Fahrbach, E. & Rohardt, G. *Physical Oceanography During POLARSTERN Cruise ANT-VIII/2 (WWGS) on Section SR02 and SR04* https://doi.org/10.1594/PANGAEA.742580 (PANGAEA, 1990).
69. Fahrbach, E. & Rohardt, G. *Physical Oceanography During POLARSTERN Cruise ANT-IX/2 on Section SR04* https://doi.org/10.1594/PANGAEA.735277 (PANGAEA, 1991).
70. WOCE Hydrographic Programme *Physical Oceanography During POLARSTERN Cruise ANT-X/4 on Section A12* https://doi.org/10.1594/PANGAEA.738488 (Alfred Wegener Institute, Hemholtz Centre for Polar and Marine Research and PANGAEA, 2002).
71. Fahrbach, E. & Rohardt, G. *Physical Oceanography During POLARSTERN Cruise ANT-X/7 on Section SR04* https://doi.org/10.1594/PANGAEA.742651 (PANGAEA, 1993).
72. Fahrbach, E. & Rohardt, G. *Physical Oceanography During POLARSTERN cruise ANT-XIII/4 on Section S04A* https://doi.org/10.1594/PANGAEA.738489 (PANGAEA, 1996).
73. Fahrbach, E. & Rohardt, G. *Physical Oceanography During POLARSTERN Cruise ANT-XV/4 (DOVETAIL) on Section SR04* https://doi.org/10.1594/PANGAEA.742626 (PANGAEA, 1998).
74. Rohardt, G. & Harms, S. *Physical Oceanography During POLARSTERN Cruise ANT-XVI/2* https://doi.org/10.1594/PANGAEA.735530 (Alfred Wegener Institute, Helmholtz Centre for Polar Marine Research and PANGAEA, 2010).
75. Schröder, M. *Physical Oceanography During POLARSTERN Cruise ANT-XVIII/3* https://doi.org/10.1594/PANGAEA.742584 (Alfred Wegener Institue, Helmholtz Centre for Polar Marine Research and PANGAEA, 2010).
76. Schröder, M. & Wisotzki, A. *Physical Oceanography During POLARSTERN Cruise ANT-XX/2* https://doi.org/10.1594/PANGAEA.738486 (Alfred Wegener Institue, Helmholtz Centre for Polar Marine Research and PANGAEA, 2010).
77. Rohardt, G. *Physical Oceanography During POLARSTERN Cruise ANT-XXII/3* https://doi.org/10.1594/PANGAEA.733664 (Alfred Wegener Institue, Helmholtz Centre for Polar Marine Research and PANGAEA, 2010).
78. Fahrbach, E. & Rohardt, G. *Physical Oceanography During POLARSTERN Cruise ANT-XXIV/3* https://doi.org/10.1594/PANGAEA.733414 (PANGAEA, 2008).
79. Rohardt, G., Fahrbach, E. & Wisotzki, A. *Physical Oceanography During POLARSTERN Cruise ANT-XXVII/2* https://doi.org/10.1594/PANGAEA.772244 (Alfred Wegener Institue, Helmholtz Centre for Polar Marine Research and PANGAEA, 2011).
80. Rohardt, G. *Physical Oceanography During POLARSTERN Cruise ANT-XXIX/2* https://doi.org/10.1594/PANGAEA.817255 (Alfred Wegener Institue, Helmholtz Centre for Polar Marine Research and PANGAEA, 2013).
81. Lemke, P., Rohardt, G. & Krüger, M. *Physical Oceanography During POLARSTERN Cruise ANT-XXIX/6 (AWECS)* https://doi.org/10.1594/PANGAEA.819714 (Alfred Wegener Institue, Helmholtz Centre for Polar Marine Research and PANGAEA, 2013).
82. Rohardt, G. & Boebel, O. *Physical Oceanography Measured on Water Bottle Samples During POLARSTERN Cruise PS89* (ANT-XXX/2) https://doi.org/10.1594/PANGAEA.846773 (Alfred Wegener Institue, Helmholtz Centre for Polar Marine Research and PANGAEA, 2015).
83. Rohardt, G. & Boebel, O. *Physical Oceanography During POLARSTERN Cruise PS103 (ANT-XXXII/2)* https://doi.org/10.1594/PANGAEA.881076 (Alfred Wegener Institue, Helmholtz Centre for Polar Marine Research and PANGAEA, 2017).
84. Rohardt, G. & Boebel, O. *Physical Oceanography During POLARSTERN Cruise PS117* https://doi.org/10.1594/PANGAEA.910663 (Alfred Wegener Institue, Helmholtz Centre for Polar Marine Research and PANGAEA, 2020).

85. Schaffer, J. & Timmermann, R. *Greenland and Antarctic Ice Sheet Topography, Cavity Geometry, and Global Bathymetry (RTopo-2), Links to NetCDF Files* https://doi.org/10.1594/PANGAEA.856844 (PANGAEA, 2016).
86. Zhou, Shenjie (2023): Weddell Sea Bottom Water area timeseries along WOCE sections, A23, A12 and SR4. figshare. Dataset. https://doi.org/10.6084/m9.figshare.23214140.v1
87. Water mass area computation. *Zenodo* https://doi.org/10.5281/zenodo.7919319 (2023).
88. Sea ice concentration budget analysis. *Zenodo* https://doi.org/10.5281/zenodo.7919315 (2023).

Acknowledgements

We thank the originators of all the open-access datasets used in this study, including remotely sensed sea-ice concentration, sea-ice drift, atmospheric reanalysis datasets and climate indices. This study received funding from the European Union's Horizon 2020 research and innovation programme under grant agreement no. 821001 (SO-CHIC) and the Natural Environment Research Council (grant NE/N018095/1, ORCHESTRA, and NE/V013254/1, ENCORE). S.Ø. received funding from the European Union's Horizon 2020 research and innovation programme under grant agreement no. 820575 (TiPACCs). A.S. acknowledges the funding from NERC (NE/V014285/1).

Author contributions

S.Z. and A.J.S.M. jointly conceived the study. S.Z. performed all the data analysis, produced all figures and interpreted results. E.P.A. provided data for repeat hydrographic sections and codes for water-mass-area calculation. A.J.S.M., M.P.M., E.P.A. and S.Ø. helped with the water-mass-area interpretation. P.R.H. and A.S. provided codes needed for sea-ice-concentration budget analysis and helped with the interpretation. P.R.H. provided insights into the IPO–wind–sea-ice teleconnection. A.J.S.M., J.-B.S., M.P.M. and P.R.H. helped refine the water-mass-volume budget analysis. All authors contributed to the writing and proofreading of this manuscript.

Competing interests

The authors declare no competing interests.

Additional information

Extended data is available for this paper at https://doi.org/10.1038/s41558-023-01695-4.

Supplementary information The online version contains supplementary material available at https://doi.org/10.1038/s41558-023-01695-4.

Correspondence and requests for materials should be addressed to Shenjie Zhou.

Peer review information *Nature Climate Change* thanks Xichen Li, Ariaan Purich and the other, anonymous, reviewer(s) for their contribution to the peer review of this work.

https://doi.org/10.1038/s41558-023-01695-4

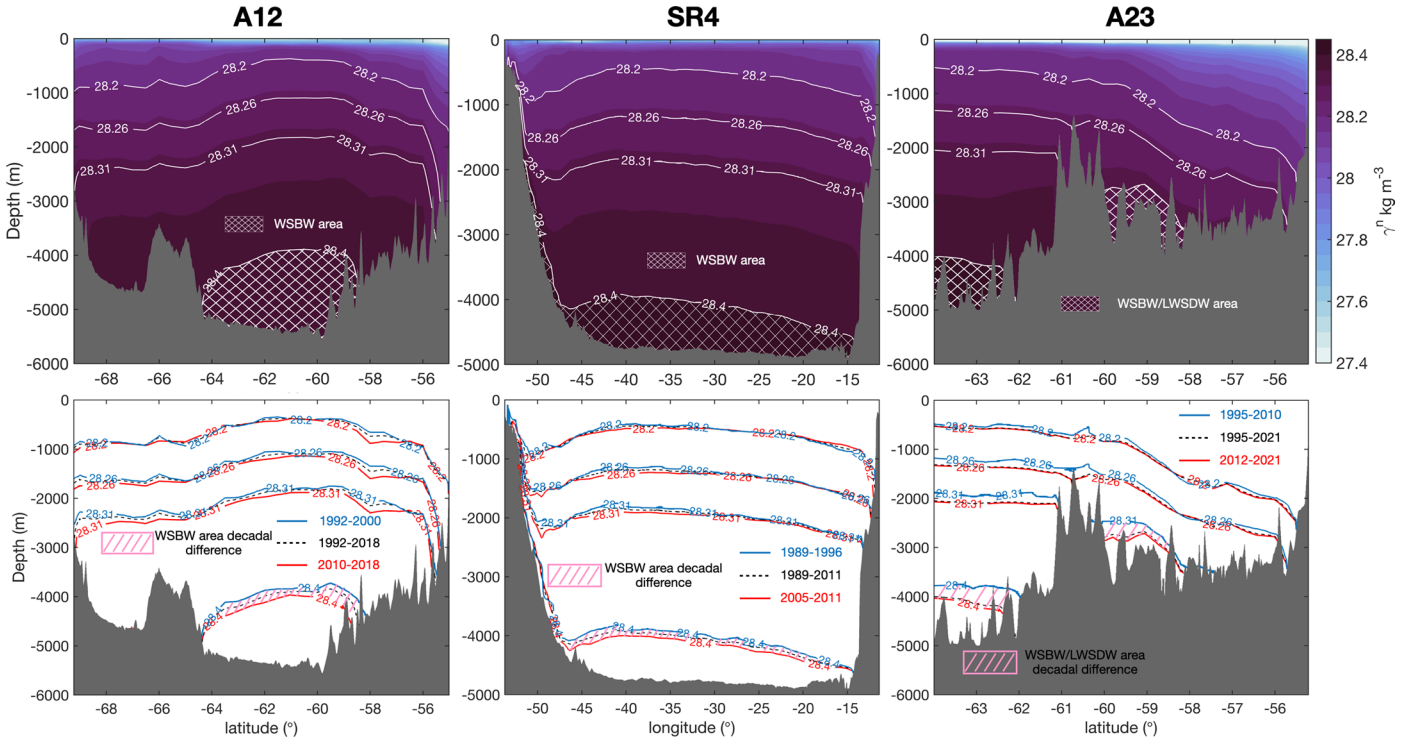

Extended Data Fig. 1 | Weddell Sea Bottom Water distribution and decadal changes. Top panels show the time mean neutral density distribution at three hydrographic transects (from left to right) A12, SR4 and A23 over approximately 1990s to 2020 (see dates below). The hatched area depicts the WSBW (A12, SR4, and A23 in the Weddell Sea) and Lower WSDW (A23 in the Scotia Sea) area at each transect averaged over time. Bottom panels show the decadal difference of the water mass area in the WSBW and Lower WSDW. Blue contours are neutral density from early years occupations on A12 (1992–2000), SR4 (1989–1996) and A23 (1995–2010). Red contours are those from later years on A12 (2010–2018), SR4 (2005–2011) and A23 (2012–2021). The periods are chosen for comparison according to the frequency of occupation of each transect to make sure two periods of comparison have a similar number of years of data available. Hatched area highlights the WSBW/Lower WSDW area difference between two periods of comparison at each transect.

https://doi.org/10.1038/s41558-023-01695-4

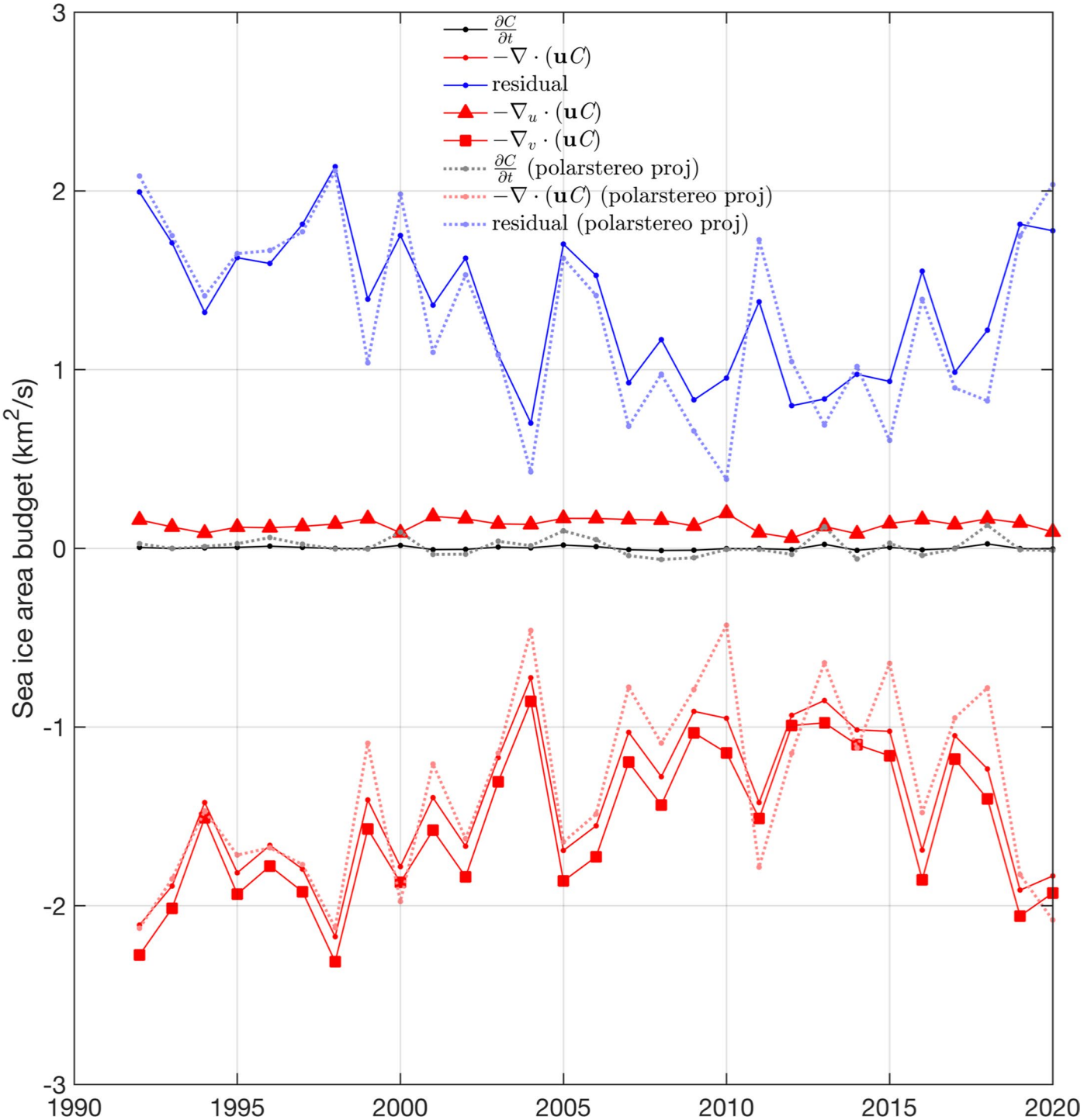

Extended Data Fig. 2 | Dynamic sea ice flux dominated by meridional components. The meridional component of sea ice dynamic flux is examined by projecting sea ice concentration and sea ice drift data from polar stereographic grid to geographical (lon-lat) grid. The solid line in the plot shows sea ice tendency analysis performed on geographical grid, colour coded in the same way as in Fig. 3d. Dashed lines are original results identical with Fig. 3d. The meridional and zonal sea ice dynamic fluxes are shown in solid red lines with square and triangle markers respectively. The meridional component dominates the total dynamic sea ice flux (solid red) that are responsible for the thermodynamic sea ice growth changes (solid blue).

https://doi.org/10.1038/s41558-023-01695-4

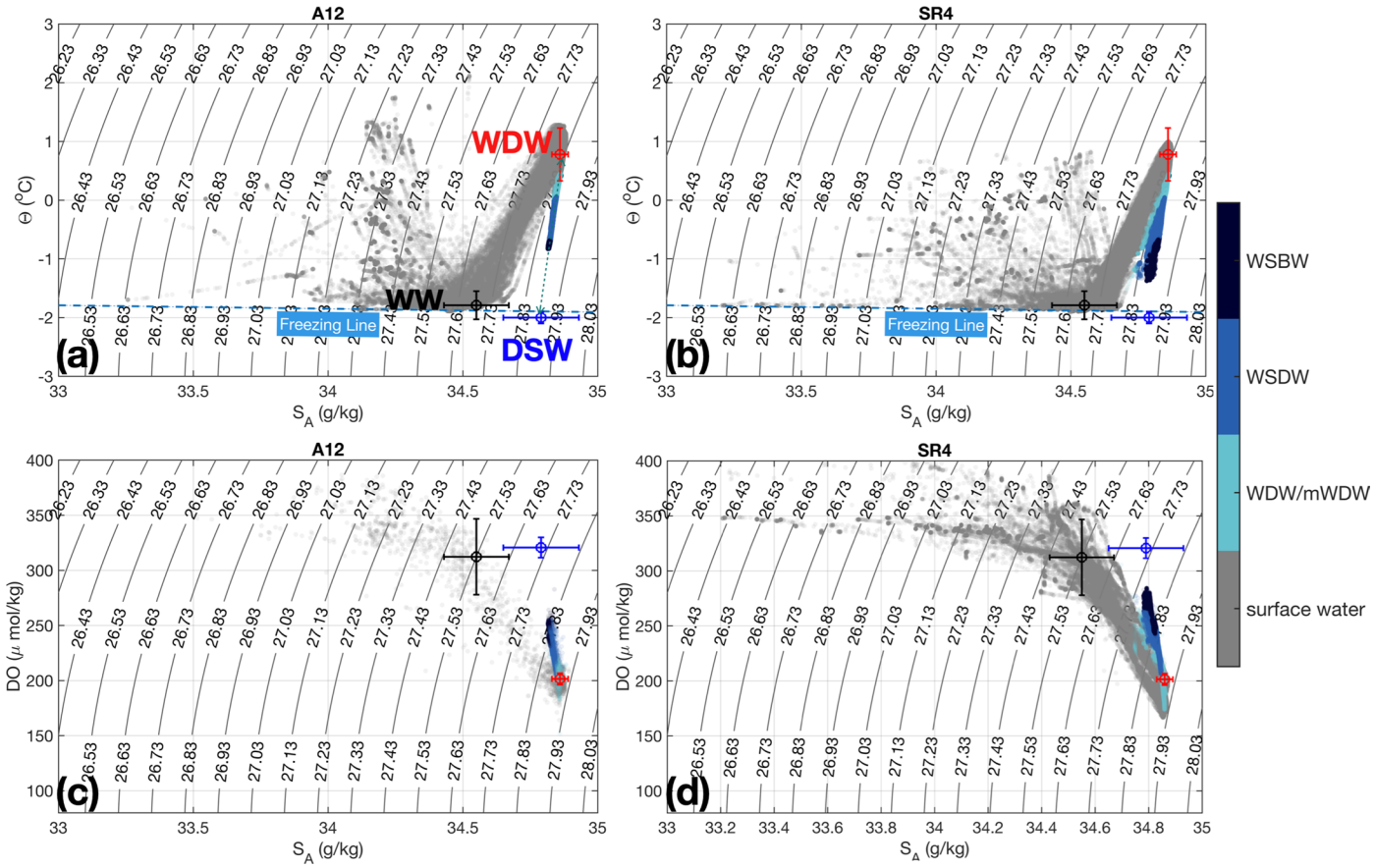

Extended Data Fig. 3 | Mixing recipe of WSBW. a,**b**, T-S plots for A12 (**a**) and SR4 (**b**). **c**,**d**, Dissolved Oxygen-Salinity (DO-S) plots for A12 (**c**) and SR4 (**d**). Typical source water types that contribute to WSBW (dark blue) are identified in T-S and DO-S space: DSW, WDW and Winter Water (WW). The WSBW data points mostly cluster in the middle along the mixing line between DSW and WDW, suggesting a roughly equal contribution to WSBW from DSW and WDW. The computation of mean properties for each source water type follows Akhoudas et al.[43], and the error bars denote ±1 standard deviation, the data used to characterise DSW and WW are selected from WAPITI cruise[43] observation over the continental shelf. For WDW, the data are selected along ANDREX/I6S section[12].

https://doi.org/10.1038/s41558-023-01695-4

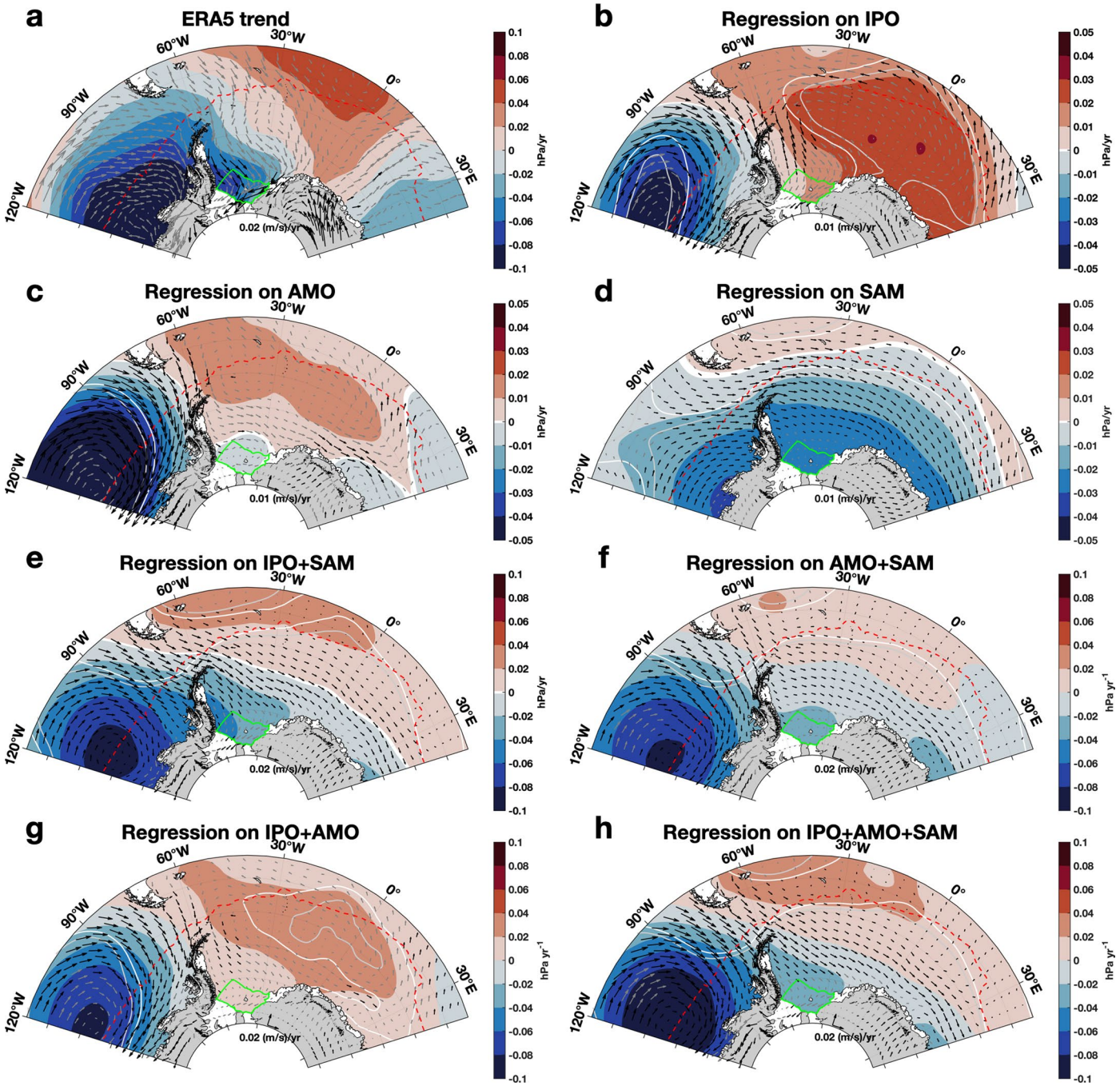

Extended Data Fig. 4 | Observed and linearly regressed surface wind trend and mean sea level pressure trend on various combinations of climatic indices. a. Observed total ERA5 trend for wind and mean sea level pressure, and **b**-**h** the regression maps on various climatic indices. **b**. Linear regression map of wind and mean sea level pressure on IPO×IPO trend. **c**. Linear regression map of wind and mean sea level pressure on AMO×AMO trend. **d**. Linear regression map of wind and mean sea level pressure on SAM×SAM trend. **e**. Multiple linear regression map of wind and mean sea level pressure on IPO×IPO trend + multiple linear regression map of wind and mean sea level pressure on SAM×SAM trend. **f**. Multiple linear regression map of wind and mean sea level pressure on AMO×AMO trend + multiple linear regression map of wind and mean sea level pressure on SAM×SAM trend. **g**. Multiple linear regression map of wind and mean sea level pressure on IPO×IPO trend + multiple linear regression map of wind and mean sea level pressure on AMO×AMO trend. h. Multiple linear regression map of wind and mean sea level pressure on IPO×IPO trend + multiple linear regression map of wind and mean sea level pressure on AMO×AMO trend + multiple linear regression map of wind and mean sea level pressure on SAM×SAM trend. All regressions are produced using data from 1979 to 2020 April-October. All the trends are estimated for April-October from 1992 to 2020.

https://doi.org/10.1038/s41558-023-01695-4

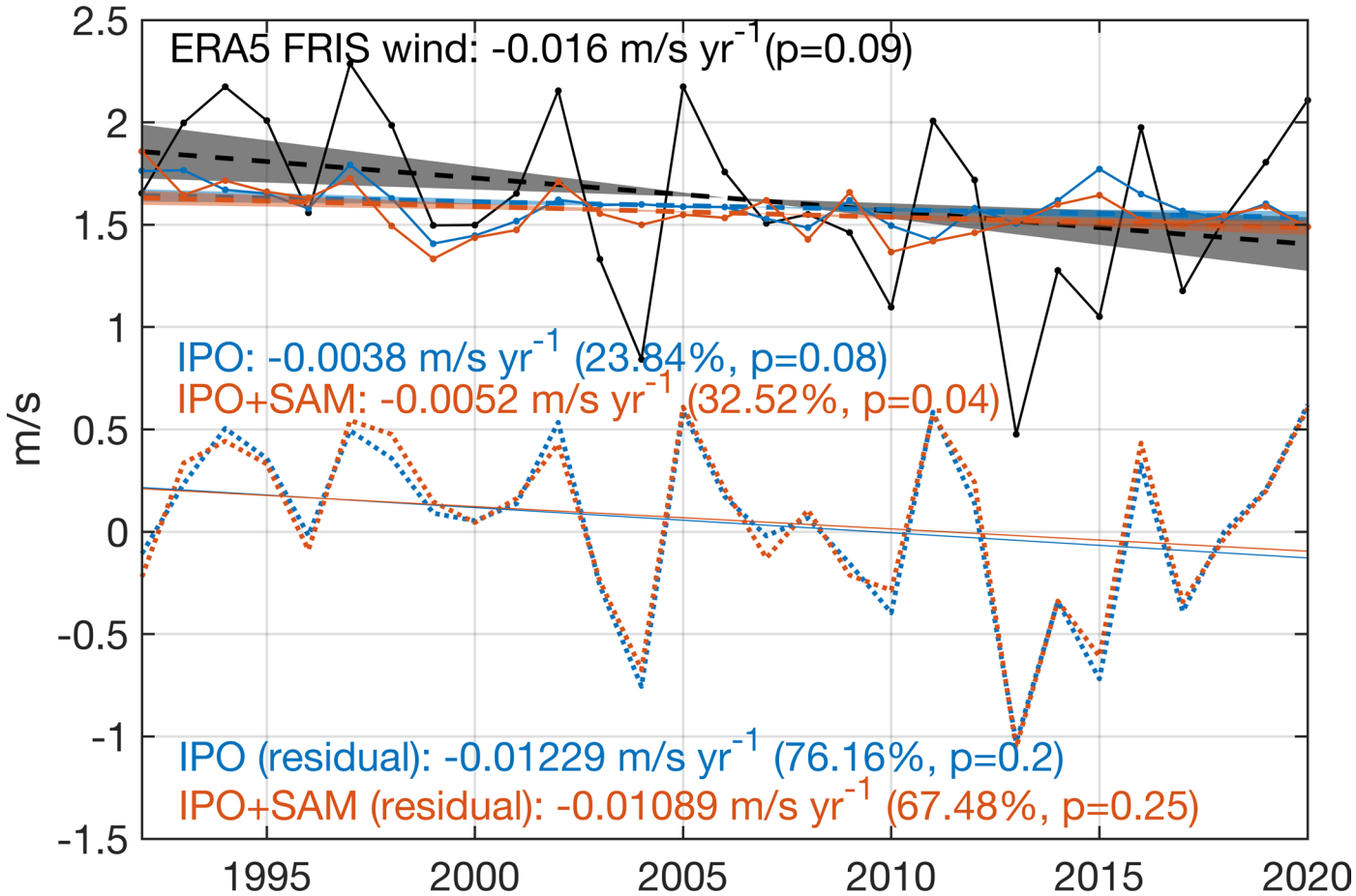

Extended Data Fig. 5 | Reconstructed FRIS meridional wind from regressions on IPO, IPO+Southern Annular Mode (SAM) against ERA5 wind. Reconstructed wind time series based on IPO (blue) and IPO + SAM (red) explain less than 10% of the total variance in ERA5 wind (black). Only 24–33% wind trend is captured by linear regression on climatic indices, while most of the variability is left in residual terms (dashed). The reconstructed wind trend is still statistically significant (>90%).

https://doi.org/10.1038/s41558-023-01695-4

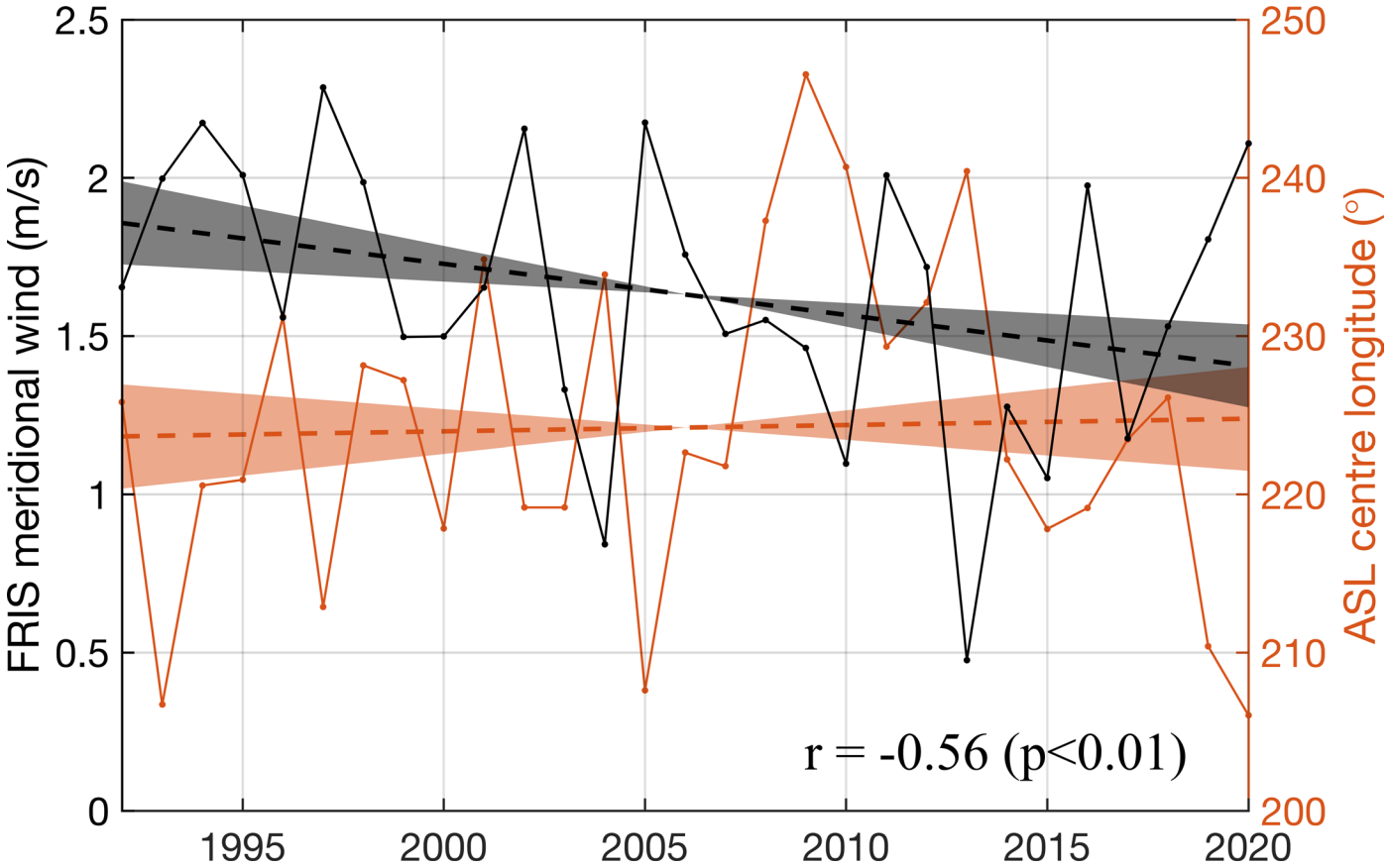

Extended Data Fig. 6 | Correlation between FRIS meridional wind and ASL position. FRIS meridional wind variability can be mostly explained by the internal fluctuation of ASL position, but the wind trend is not attributed to ASL position as its position displays an insignificant trend.

https://doi.org/10.1038/s41558-023-01695-4

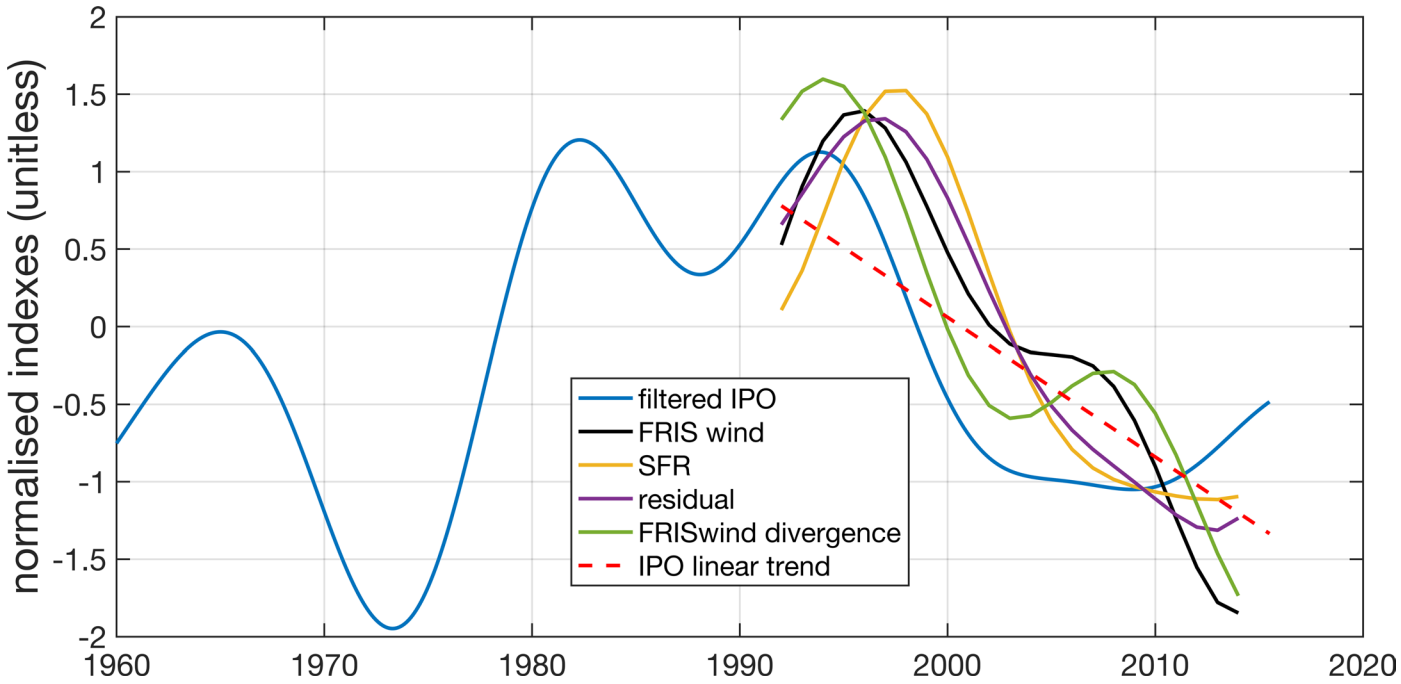

Extended Data Fig. 7 | Normalised IPO index and metrics of wind changes and sea ice. A negative polarity in IPO (blue, red dashed line show the linear trend) since early 1990 is accompanied by the decrease in meridional wind in FRIS (black) and a reduced convergence in FRIS wind (green). Both sea ice formation rate (yellow) and thermodynamic ice growth (violet) experience a declined trend over the same examining period. All time series are low-pass filtered with a 13-year cut-off frequency.

https://doi.org/10.1038/s41558-023-01695-4

Extended Data Table 1 | Weddell Sea and global ocean warming rate at different depth ranges

Depth range	Warming rate (W m-2)	
	Weddell Sea (% explained by HVE)	**Global Ocean**
0 m – bottom	0.67±0.27 (71%)	0.71±0.09
2000 m – bottom	0.34±0.18 (90%)	0.07±0.06
0 – 700 m	0.00±0.82 (40%)	0.31
700 – 2000 m	0.33±0.30 (99%)	0.34

The warming rate in the global ocean is taken from Desbruyères et al.[37]. Weddell Sea warming rate is computed from temperature trends estimated from A12, SR4 and A23 (Weddell parts) assuming a uniform warming rate at the same depth for simplification. Percentage of warming rate explained by isopycnal heaving is also listed. The deep Weddell warming (> 2000 m) is 5 times of the global average, consistent with Strass et al.[34], and mostly explained by the isopycnal heaving.